

Thermal and Electrical Properties of Multiwall Carbon Nanotubes

Wei Yi

Thesis Advisor:
Prof. Li Lu

Institute of Physics
Chinese Academy of Sciences

June 1999

submitted in partial fulfillment of the requirements for the degree of
Master of Science
in the subject of
Condensed Matter Physics

学位论文

分类号_____ 密级_____

UDC _____ 编号_____

中国科学院物理研究所

研 究 生 学 位 论 文

题目: 多层碳纳米管的热学和电学性质

Title: Thermal and Electrical properties of Multiwall Carbon Nanotubes

姓名: 易伟

导师: 吕力 研究员

申请学位级别: 理学硕士

专业名称: 凝聚态物理

论文提交日期: 1999 年 6 月

论文答辩日期: 1999 年 6 月

学位授予单位和日期: 中国科学院物理研究所

答辩委员会主席: _____

评阅人: _____

1999 年 6 月

©1999 - Wei Yi

All rights reserved.

摘要

本文利用有机气体催化热解法制备的毫米长的取向多层碳纳米管，对它的热学和电学性质进行了详细研究。本文共分六章。第一章为绪论，扼要概述了碳纳米管的发现、结构、性质（包括理论研究和实验研究）。第二章概述了有机气体催化热解法制备毫米长取向多层碳纳米管的制备工艺和表征。在第三章中，利用一种新的自加热 3ω 方法测量了碳纳米管的热导、比热和热扩散系数。发现直径为几十纳米的多层碳纳米管的比热在全部测量温区（10—300K）随温度呈很好的线性关系。该结果显示多层碳纳米管的层间耦合比石墨的弱得多，因此在热学性质上多层碳纳米管可以看作弱耦合的二维单层管的集合。热导率在高于120K的温区随温度大致呈线性关系，而低于120K则呈二次方关系。热导率的幅值较低，反映出热解法制备的多层碳纳米管可能存在较多的缺陷。在第四章中，首次用四点法测量了多层碳纳米管和正常金属之间的单隧道结的低温隧道谱。观察到隧道态密度的强烈“零偏压抑制”现象，表现为隧道结微分电导随偏压和温度的幂次率关系。利用环境量子涨落理论对微分电导随偏压和温度的关系进行了定量拟合，发现幂次率指数是个由碳纳米管内库仑作用强度决定的普适常数。在两个有较小的结阻抗的样品中，发现在温度低于1K且偏压小于1mV的区域，隧道电导出现呈Fano线型的非对称共振峰，该现象可以用开放的量子点中的Kondo物理来解释。在第五章中，对多层碳纳米管的热电势和纵向磁阻进行了研究。利用比较法测量了碳纳米管的热电势。发现碳纳米管有比较大的正热电势，在低温区（小于大约100K）随温度呈很好的金属性的线性关系。这样一个大的正热电势与石墨完全不同，可能意味着金属性碳纳米管中由于缺陷等可能的机制导致电子—空穴对称性的破缺。在20mK的极低温下测量了碳纳米管的纵向磁阻。发现电阻随磁场增加呈现很好的周期性振荡行为。如果只考虑最外层管壁对电导的贡献，则振荡周期与具有 $h/2e$ 周期的Altshuler-Aronov-Spivak（AAS）效应一致。该结果清晰地反映出低温下多层碳纳米管中的量子相干行为，利用理论拟合得出的相位相干长度与最外层管子的周长相当。第六章为结论。

关键词：石墨，碳纳米管，比热，热导， 3ω 方法，隧道谱，库仑作用，Fano共振，热电势，磁阻，AAS效应，量子相干

Abstract

In this dissertation, extensive researches on the thermal and electrical properties of millimeter-long aligned multiwall carbon nanotubes (MWNTs) prepared by thermal decomposition of hydrocarbons have been presented.

The thesis consists of six chapters. Chapter 1 is an introduction, in which the discovery, structure and physical properties (including theoretical and experimental) are outlined. In Chapter 2, the preparation techniques and the characterizations of the carbon nanotubes are described.

In Chapter 3, by using a novel self-heating 3ω method, the specific heat, diffusivity coefficient and thermal conductivity of MWNTs are for the first time reported. MWNTs of a few tens nm diameter is found to demonstrate a strikingly linear temperature-dependent specific heat over the entire temperature range measured (10–300 K). The results indicate that inter-wall coupling in MWNTs is rather weak compared with in its parent form, graphite, so that one can treat a MWNT as a few decoupled two-dimensional (2D) single wall tubules. The thermal conductivity κ of MWNTs has a roughly linear temperature dependence above ~ 120 K, below ~ 120 K, κ follows almost a quadratic T -dependence. The room-temperature amplitude of κ is found to be low, indicating the existence of substantial amount of defects in the MWNTs prepared by chemical-vapor-deposition method.

In Chapter 4, the first true four-probe measurement of tunneling spectroscopy for single tunnel junctions formed between MWNTs and a normal metal is presented. The intrinsic Coulomb interactions in the MWNTs give rise to a strong zero-bias suppression of tunneling density of states (TDOS) that can be fitted numerically with the environmental quantum-fluctuation (EQF) theory. At low temperatures, an asymmetric conductance anomaly near zero bias is observed, which is interpreted as Fano resonance in the strong tunneling regime.

In Chapter 5, the thermoelectric power (TEP) and longitudinal magnetoresistance (MR) of MWNTs are measured. MWNTs have a moderately large positive TEP. At low temperatures, TEP has a metallic-like linear temperature dependence. The results give strong evidence that the electron-hole symmetry in metallic nanotubes is broken. The longitudinal MR of MWNTs is measured at 20 mK. Periodic oscillations are observed when a longitudinal magnetic field is applied. If only the outermost graphene wall of MWNTs contributes to electrical conductance, the period of oscillation agrees well with the period

$h/2e$ of Altshuler-Aronov-Spivak (AAS) effect. The present results clearly indicate that quantum-interference dominate the resistance of MWNTs at low temperatures.

Chapter 6 presents the main conclusions of this thesis.

Keywords: graphite, carbon nanotubes, specific heat, thermal conductivity, 3ω method, tunneling spectroscopy, Coulomb interactions, Fano resonance, thermoelectric power, magnetoresistance, AAS effect, quantum interference

Contents

Title Page	i
Abstract	v
Table of Contents	vii
Publication List	ix
Dedication	x
1 Introduction	1
1.1 Discovery of carbon nanotubes	1
1.2 Structure	2
1.3 Physical properties, theoretical	4
1.4 Physical properties, experimental	8
1.5 Motivation and goal	10
Bibliography	12
2 Sample growth and characterization	16
2.1 Introduction	16
2.2 Process of synthesis	16
2.3 Characterization	18
2.4 Summary	23
Bibliography	25
3 Thermal properties	26
3.1 Introduction	26
3.2 Experimental	26
3.3 Results and discussion	29
3.4 Summary	35
3.5 Appendix: 3Ω method	35
3.5.1 Solution of the 1D heat-conduction equation in the presence of an AC heating current	37
3.5.2 Experimental test	42
3.5.3 Summary	48
Bibliography	49

4	Tunneling Spectroscopy	53
4.1	Motivation	53
4.2	Experimental	54
4.3	Discussion	56
4.4	Fano resonance	59
4.5	Summary	62
	Bibliography	63
5	Transport Properties	65
5.1	Thermoelectric power	65
5.1.1	Introduction	65
5.1.2	Experimental	66
5.2	Magnetoresistance	69
5.3	Summary	72
	Bibliography	73
6	Conclusions	74
	Acknowledgments	77
	Revision Notes	78

Publication List

1. W. Yi, L. Lu, Zhang Dian-lin, Z. W. Pan, and S. S. Xie, *Linear specific heat of carbon nanotubes*, *Phys. Rev. B* **59**, R9015 (1999).

2. L. Lu, W. Yi, and Zhang Dian-lin, *A 3ω method for both specific heat and thermal conductivity measurement*, in preparation. (Published as: L. Lu, W. Yi, and D. L. Zhang, *3-omega method for specific heat and thermal conductivity measurements*, *Rev. Sci. Instrum.* **72**, 2996 (2001).)

3. W. Yi, L. Lu, Zhang Dian-lin, Z. W. Pan, and S. S. Xie, *Electron-electron correlations in multiwall carbon nanotubes detected by tunneling spectroscopy*, in preparation. (Published as: W. Yi, L. Lu, H. Hu, Z. W. Pan, and S. S. Xie, *Tunneling into Multiwalled Carbon Nanotubes: Coulomb Blockade and the Fano Resonance*, *Phys. Rev. Lett.* **91**, 076801 (2003).)

Dedicated to my parents

Chapter 1

Introduction

1.1 Discovery of carbon nanotubes

Carbon is really a special element in nature, whose chemical versatility makes it the central agent in most organic and inorganic chemistry as well as the fundamental constituent of all biological systems.

Until recently, pure carbon was only known to exist in two forms: diamond and graphite. In 1985, Harold Kroto, Robert Curl and Richard E. Smally discovered a new form of carbon—the fullerenes, which are molecules of pure carbon atoms bonded together forming geometrically regular structures [1]. The best-known of these is C_{60} , which has precisely the same geometry as a soccer ball, with one carbon atom at each point where the seams intersect. Because its structure is similar to that of the geodesic dome developed by the American architect, Buckminster Fuller, so this new molecule was named buckminsterfullerene, or buckyball. The discovery of fullerenes has added an important milestone in carbon research.

Most importantly, research has proven the possibilities for producing a whole new range of carbon structures of various sizes, shapes and dimensionalities. According to Euler theorem, infinite kinds of closed cage structure can be made by add a minimum number of 12 pentagons to carbon honeycomb lattices. Soon later people discovered various such structures, such as C_{70} , C_{76} , C_{84} , C_{96} , etc. Naturally, the possibility of existence of tube-sized fullerene molecules, i.e., carbon nanotubes, has also been proposed.

In 1991, S. Iijima firstly observed the existence of carbon nanotube while studying the surface of carbon electrodes used in an electric arc-discharge apparatus which had been

used to make fullerenes [2]. He found needle-like carbon whiskers with diameter of 4–30 nm and length of 1 μm . These carbon whiskers are hollow tubes made of concentric clinders of carbon honeycomb lattices. The distance between adjacent cylinders is similar to inter-layer distance of graphite, i.e., $d \sim 0.34$ nm. The discovery of carbon nanotubes stimulated tremendous interest in scientific community immediately. The subsequent success of the large-scale synthesis of nanotubes by T. W. Ebbesen and P. M. Ajayan of NEC opened the door for their widespread study. In 1993, Iijima [3] and D. S. Bethune [4] firstly observed single-wall carbon nanotubes (SWNTs) with diameter only ~ 1 nm. The relative simplicity of structure of SWNTs made them suitable for theoretical calculations. By 1996, A. Thess successfully synthesized large quantities of high-quality SWNTs using pulsed laser evaporation technique [5]. Taking advantage of Scanning Probe Microscopy techniques obtainable nowadays, experimental explorations on the properties of individual SWNT made rapid progress, which has found extremely good agreement with theoretical predications.

1.2 Structure

Carbon nanotubes are made up of one or more wrapped-up seamless cylinders of carbon honeycomb lattices. The theoretically smallest nanotubes have a diameter equal to that of C_{60} ($d = 0.7$ nm), which could be thought as two hemispheres of C_{60} connected by a single wrapped-up graphite sheet. If a C_{60} molecule is separated perpendicular to the quintic symmetry axis, the derived tube is called ‘armchair’ (Fig. 1.1 a); if it is separated perpendicular to the cubic symmetry axis, the derived tube is called ‘zigzag’ (Fig. 1.1 b). We can see that the orientation of carbon hexagonal rings is either parallel or vertical to the tube axis for these two kinds of tubes. Actually for most of the nanotubes, the orientation of hexagonal rings is neither parallel nor vertical to the tube axis, but has some fixed helical angel. Such nanotubes have chirality (Fig. 1.1 c).

In 1992, Hamada et al. developed an indexing method to represent the structure for single shell of carbon nanotubes [7]. As shown in Fig. 1.2 a, carbon atoms are located at the corners of honeycomb lattice. The two primitive lattice vectors are $\vec{a}_{1,2} = (a/2)(\pm 1, \sqrt{3})$, where $a = \sqrt{3}d$, with $d = 0.1421$ nm is the nearest-neighbour carbon separation. All the possible structures of carbon nanotubes can be represented by a pair of integers (n, m). A (n,

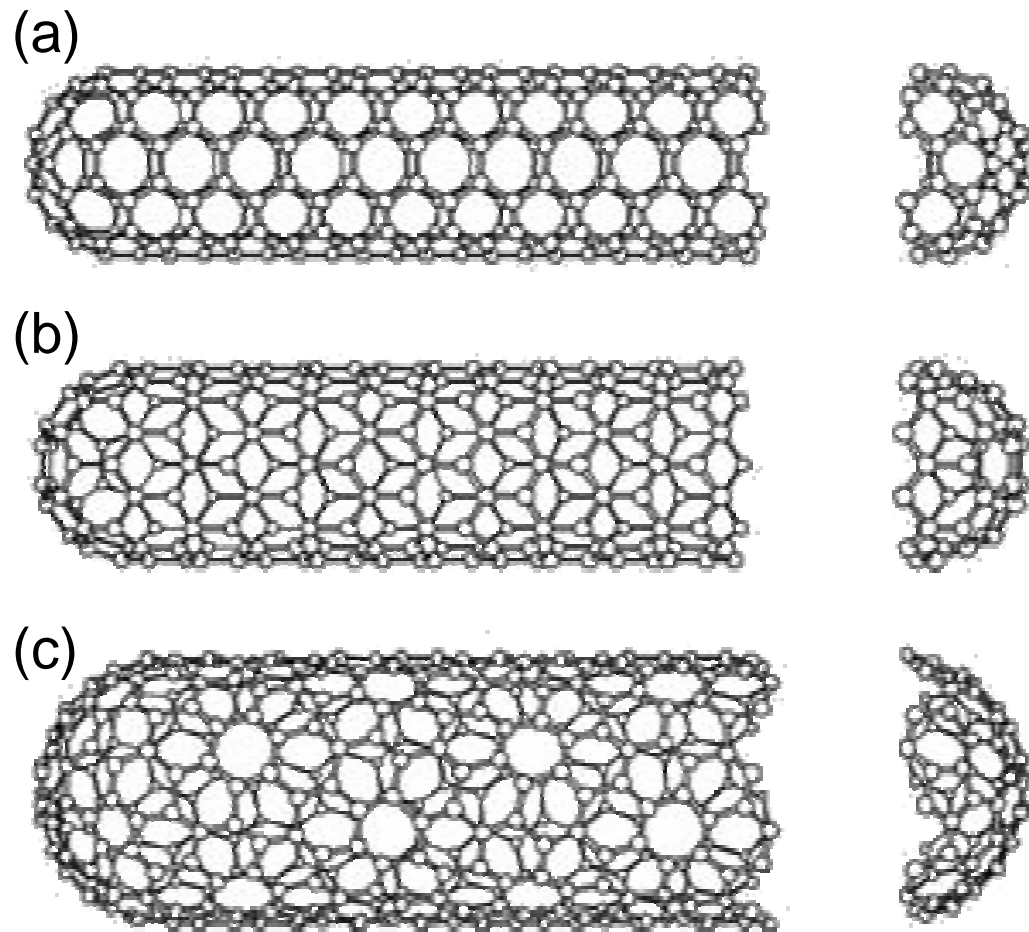


Figure 1.1: Schematic of the formation of carbon nanotubes by wrapping up graphene sheet. Different means of wrapping produce different tube structures: (a) armchair, (b) zigzag, (c) chiral. From Ref. [6]

m) nanotube is made by folding the two-dimensional hexagonal lattice shown and matching the lattice point (n, m) with the origin, with a wrapping vector $\vec{C} = n\vec{a}_1 + m\vec{a}_2$. If we define the wrapping orientation of zigzag nanotube as the reference axis, the separation angle between the wrapping vector \vec{C} and the reference axis is the helical angle θ . All nanotubes are uniquely defined by the helical angle θ and the distance $|\vec{C}|$ which defines the tube size. Because of the symmetry of graphite lattice, θ is chosen as $0 < \theta < 30^\circ$ to avoid duplicity. The three kinds of nanotubes have different helical angle θ . For armchair tubes, $n = m$, $\theta = 30^\circ$. The zigzag tubes correspond to $m = 0$ and $\theta = 0$. When $n \neq m$ and not equal to zero, they are helical or chiral tubes with $0 < \theta < 30^\circ$.

For a (n, m) carbon nanotube, the diameter d and helical angle θ are given by

$$d = \frac{\sqrt{3}}{\pi} a_{c-c} (n^2 + nm + m^2)^{\frac{1}{2}} \quad (1.1)$$

$$\theta = \arctan \sqrt{3}/(m + 2n) \quad (1.2)$$

1.3 Physical properties, theoretical

Carbon nanotubes as a novel quasi one-dimensional material has stimulated great interest. From theoretical point of view, singlewall carbon nanotubes is ideal for study because of their relative simplicity. A straight-forward tight-binding calculation is based on the zone-folding picture, which deduces the band structure of carbon nanotubes from their parent form, graphene sheet, with periodic boundary conditions around circumference of nanotubes [7–11]. For a graphene sheet, each atom has one conduction electron in the $2p_z$ state. The first Brillouin zone (BZ) is a hexagon whose sides are distant $1/3a_{c-c}$ from its center. It is easily shown that this zone contains one electron per atom, so graphite is a half-filling semiconductor with zero gap, or a semimetal (shown in Fig. 1.3). Fermi surface reduces into six points at the corner of hexagonal BZ. Near Fermi level, the dispersion relation is nearly linear [12].

The periodic boundary conditions around circumference of nanotube make the crystal momentum transverse to the tube axis quantized. The allowed electronic states are restricted to those in the graphene BZ that satisfy [9]

$$\vec{k} \cdot \vec{C} = 2\pi m \quad (1.3)$$

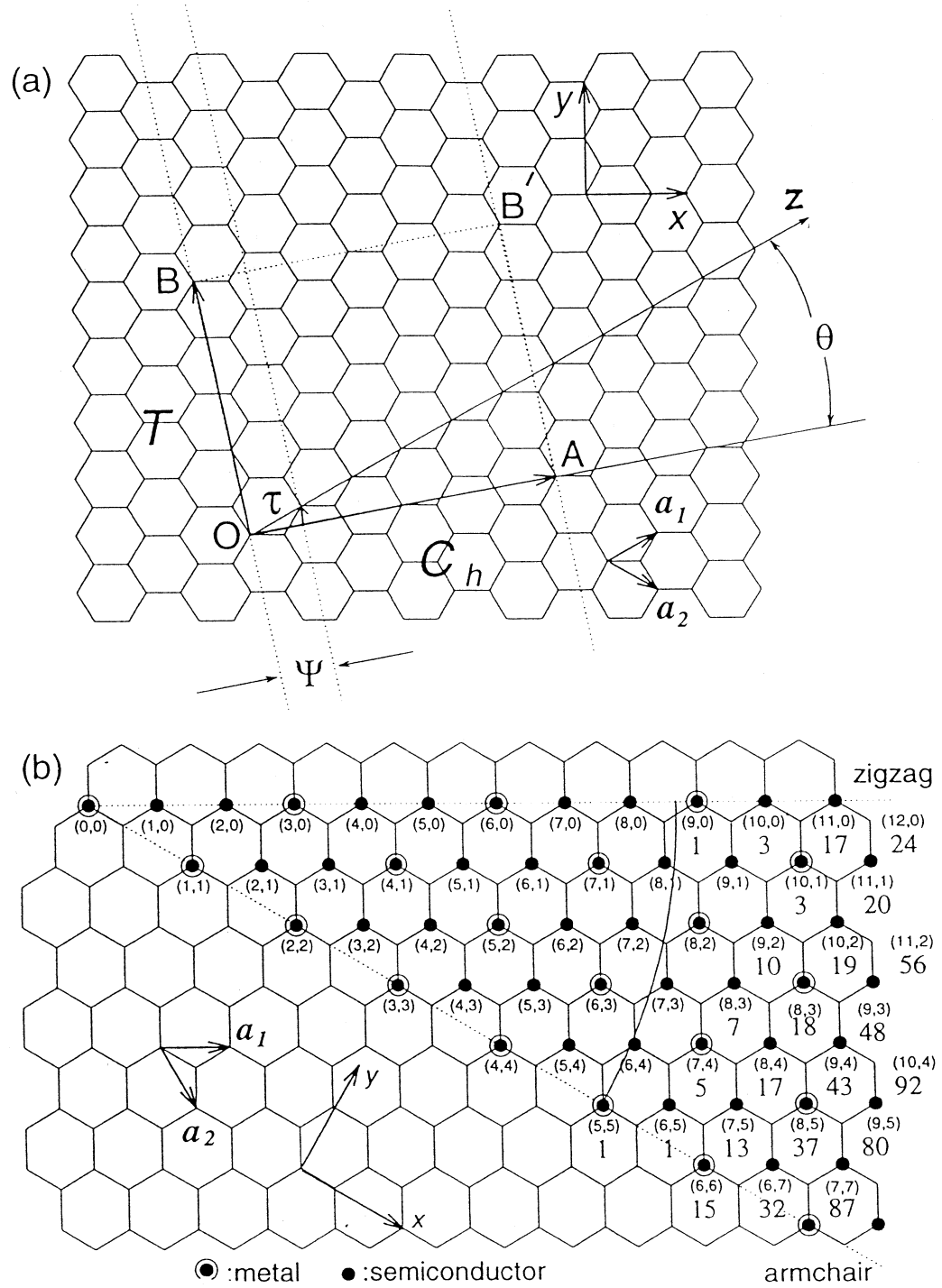


Figure 1.2: Schematic of the indexing method developed by Hamada et al. for single shells of carbon nanotubes. For example, a (6,3) nanotube is made by folding the two-dimensional hexagonal lattice shown and matching the lattice point (6,3) with the origin. The directions along which lattice points would make armchair and zigzag nanotubes are indicated. From Ref. [6]

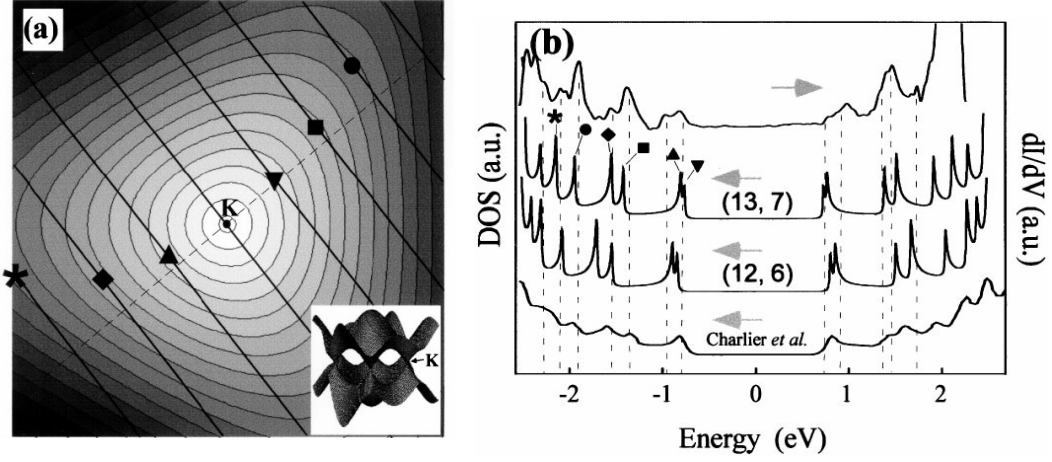


Figure 1.3: (a) Energy dispersion of the π -band of graphene sheet near the K . The solid lines correspond to 1D bands obtained by the zone-folding. Symbols are located at the positions where Van Hove singularities occur in these 1D bands. The inset depicts a three dimensional view of graphene π/π^* bands. (b) Comparison of the electron density of states obtained from scanning tunneling microscopy experiment (upper curve) and tight-binding calculations (lower curves). From Ref. [13]

with m an integer (Fig. 1.4). In terms of the two-dimensional BZ of graphene, the allowed states will lie along parallel lines separated by a spacing of $2\pi/|\vec{C}|$. Metallic behavior happens whenever the gapless Fermi points lie on the allowed transverse quantized wave vectors. For (n, n) armchair nanotubes, the gapless modes are present at $k_y = 0$, resulting in metallic behavior independent of n . For zigzag or chiral tubes with (n, m) , metallic behavior happens only if the vectors of Fermi points satisfy Eq. (1.3), leading to the condition $n - m = 3q$, where q is an integer. For the nonmetallic case, the smallest band gap for the nanotube will occur at the nearest allowed point to \vec{K} , the Fermi wavevector, with amplitude given by tight-binding Hückel model [9]

$$E_g = V_{pp\pi}d/R \quad (1.4)$$

where $V_{pp\pi}$ is hopping matrix element of the π -bands, R is the nanotube radius ($R = |\vec{C}|/2\pi$).

This simplified model does not consider the symmetry breaking introduced by curvature effects. Due to curvature effects, the Fermi points will be shifted slightly along k_x , but leaves the armchair tube gapless (Fig. 1.4a). For chiral tubes which satisfy $n - m = 3q$, Fermi points are shifted away from the allowed quantized wave vectors slightly by order of $1/R^2$. Thus chiral tubes are quasimetallic with second-order small band gaps (Fig.

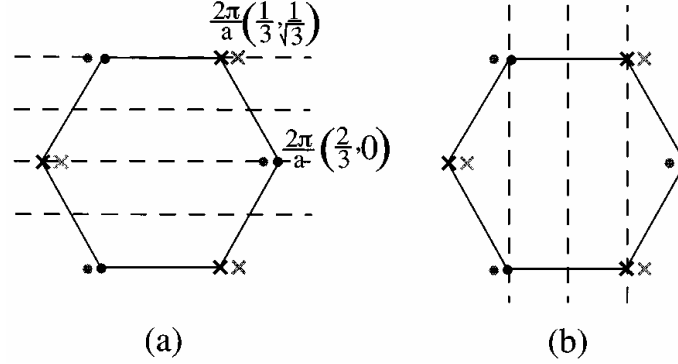


Figure 1.4: Fermi points in the Brillouin zone of carbon nanotubes. Dark circles and crosses indicate the locations of the gapless points without curvature-induced symmetry breaking, while gray symbols schematically indicate the shifted positions for curvature effects. Dashed lines cut the zone at a discrete set of allowed transverse momenta in (a) the armchair tube and (b) the zig-zag tube (here with $N=3$). From Ref. [15]

1.4b) [14, 15].

From above discussion, the armchair nanotube could be treated as truly 1D metal. The low-energy conduction modes occur near the two gapless Fermi points $\pm \vec{K} = \pm \frac{2\pi}{a}(\frac{2}{3}, 0)$. Excitation of other transversal modes costs the energy $\approx 10 \text{ eV}/n$, and hence a 1D condition arises. For (10, 10) tubes, the conditions for the low-energy regime are met even at room temperature. Up to energy scales $\sim 1 \text{ eV}$, the dispersion relation around the Fermi points remains nearly linear (Fig. 1.5 a) and cause a finite and constant density of states (DOS) near E_F (Fig. 1.5 b).

Based on studies of the electronic structures of SWNTs, theoretists also carried out some elementary studies on electronic structures of MWNTs [17–19]. It was argued that a two-layer MWNT constituted by two concentric metallic (or quasimetallic) SWNTs is still metallic (or quasimetallic). An interesting result is, when one of the metallic nanotube is replaced by a semiconducting nanotube, a concentric metal-semiconductor device could be constitute [20]. But there also exists result that indicating changes of electronic properties due to inter-layer interactions when two SWNTs joined together.

Another important research area is on the Mechanical properties of carbon nanotubes. It is well-known that the in-plane C–C covalent bond in graphite is one of the strongest bonds in nature. The best estimate of the in-plane elastic modulus is 1.06 TPa and that of the tensile stiffness is 0.8 TPa. The mechanical properties of ideal carbon nanotubes with negligible number of structural defects should approach or even surpass the

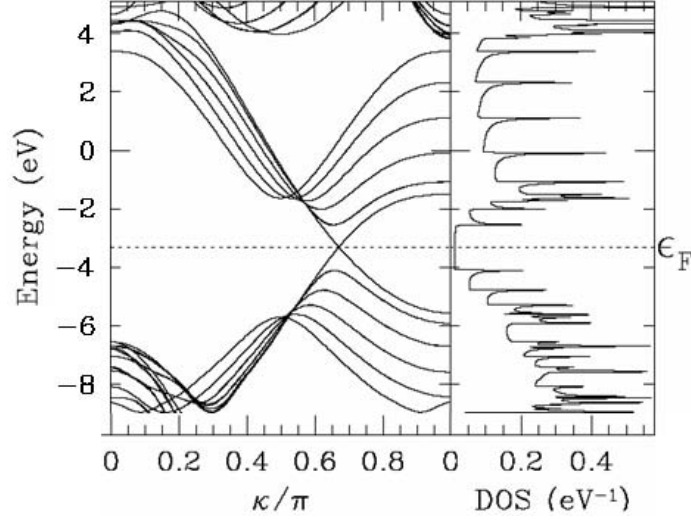


Figure 1.5: (a) Schematic of the electronic structure of (10,10) armchair nanotubes. (b) Corresponding finite and constant DOS near E_F . The ‘gap’ associated with DOS peaks at next one-dimensional subbands. From Ref. [16]

reference values of graphite. Moreover, the rolled-up structure of carbon nanotubes would make them withstand repeated bending, buckling, twisting and compression at high rates with complete elasticity.

The hollow structure of carbon nanotubes make it possible to fill them with other materials to form one-dimensional nano-wires. Theoretical studies point out that only materials with small enough surface tension could be filled into carbon nanotubes, including all the gases and liquids, most of the organic materials and some of the metals and their compounds [21–23].

1.4 Physical properties, experimental

Although numerous theoretical calculations have predicted many novel physical and chemical properties for carbon nanotubes, the nanometer size and random orientations of nanotube samples make it extremely difficult to examine and certify these properties experimentally. However, taking advantage of the rapid progress of nano-fabrication and nano-manipulation, scientists are making fast progress on experimental studies and many valuable results has been obtained which agree quite well with theoretical predictions.

Since nanotubes are ideal model systems for the investigation of low-dimensional

molecular conductors, measuring the electronic properties of individual nanotubes is always the focus of experimental studies. This is very challenging for two reasons. Both high-quality nanotube samples and new techniques for making electrical contacts to individual tubes are necessary. The first to be studied was individual multiwall nanotubes. By using STM lithography technique, Langer et al. reported the first measurement on individual MWNTs [24]. They found that transport properties of MWNTs were consistent with the quantum transport behaviors of weakly disordered low-dimensional conductors. Ebbesen et al. systematically measured four-probe conductance of individual MWNTs and observed both metallic and non-metallic behaviors [25]. Typical temperature dependence of the resistance of metallic tubes was similar to that of disordered semi-metallic graphite, with a moderate negative temperature coefficient. Another elegant method of electrical contact was used by Frank et al. [26]. A single MWNT attached to a STM tip was repeatedly immersed and pulled out of a liquid metal like mercury. Astonishingly, an almost universal quantized conductance at room temperature was measured, providing evidence that transport in MWNTs is ballistic over distances of the order of $\geq 1 \mu\text{m}$. Recently, a pronounced Aharonov-Bohm resistance oscillation was observed by Bachtold et al. [27]. Their results clearly demonstrate that at low temperatures quantum interference phenomena dominate the magnetoresistance of MWNTs.

Singlewall nanotubes have well defined structures and relatively less defects. The success of synthesis of high-quality SWNTs with uniformed structures greatly stimulated experimental studies. The first results on individual SWNTs were obtained by Tans et al. [28]. At low temperatures step-like current-voltage characteristics were observed that indicate single-electron transport with Coulomb blockade and resonant tunneling through single molecular orbitals. Quite remarkably, the nanotubes appear to behave as coherent quantum wires. The density of states of the molecule consist of well-separated discrete electron states corresponding to an one-dimensional ‘particle-in-a-box’ situation induced by micrometer tube length. The measurement on individual SWNT ropes by Bockrath et al. [29] obtained similar results. Soon later, two research groups at Delft Univ. and Harvard Univ. obtained the first atomic resolution STM images of SWNTs and observed the chiral winding of the hexagons along the tube [30, 31]. The STM was also used to measure the tunneling spectroscopy of nanotubes. They found both metallic and semiconducting spectra. Their data provided the first experimental verification of the bandstructure predictions. The observed gap structures quantitatively agree with the calculations.

The explanations of all these experiments were based on single-electron picture, wherein the Landau Fermi liquid theorem is appropriate. However, the low-dimensional nature of carbon nanotubes would probably introduce pronounced electron-electron interactions, and a non-Fermi liquid behavior such as a Luttinger Liquid is predicted [32–35]. The first generation devices used in transport measurement of individual SWNTs have very high contact resistance, therefore the effect of electron-electron correlations was masked by charging effects. Tans et al. exhibited the first evidence of electron correlations by finding that electrons tunneling into a SWNT are spin polarized [36]. By improving the quality of electric contact, Bockrath et al. recently observed a power-law suppression of tunneling DOS on individual SWNT ropes [37], which could be well explained by tunneling into the bulk and ends of a clear Luttinger Liquid.

The experimental characterizations of mechanical properties of carbon nanotubes is very difficult because of the short length (1–100 μm) of the samples. Up to now, there are no direct tensile tests available to determine the axial strength of nanotubes. By measuring the amplitudes of intrinsic thermal vibrations of nanotubes during imaging inside a Transmission Electron Microscope (TEM), Treacy et al. estimated a Young's modulus as high as 1.8 TPa which is higher than the in-plane modulus for single-crystal graphite [38]. Recently, Pan et al. reported the first direct tensile test on MWNTs [39]. In their experiment, a tiny stress-strain puller was used to pull a MWNT bundle containing several ten thousand millimeter-long aligned nanotubes, and the average Young's modulus and tensile strength obtained were 0.45 ± 0.23 TPa and 1.72 ± 0.64 GPa, respectively. The relatively lower Young's modulus was attributed to the existence of large amounts of defects in CVD derived nanotubes, but it is still higher than that of Steel. Moreover, TEM observations have shown that carbon nanotubes could sustain extreme strain without showing signs of brittleness, plastic deformation or atomic rearrangements and bond rupture [40, 41]. The flexibility is related to the ability of the carbon atoms to rehybridize. All these results indicate that nanotubes do have exceptional mechanical properties.

1.5 Motivation and goal

Despite the fast progress in the researches of carbon nanotubes, many important physical properties, such as thermal properties, have not been well experimentally characterized. Success of the synthesis of millimeter-long aligned multiwall carbon nanotubes

opened the door of macroscopic manipulations on these nano-sized materials [42]. The continuity and good alignment of nanotubes enable us to perform measurements on well-defined samples. This dissertation aims at a systematic investigation on MWNTs, including their thermal properties, tunneling spectroscopy and electrical transport properties.

On thermal properties, our goal is to explore the dimensionality of the phonon structure and its relationship with tube diameter. A potential rewarding experiment would be to measure the specific heat and thermal conductivity of a small sample simultaneously. Fortunately, a so-called 3ω method, which uses a narrow-band technique in detection, and therefore gives a relatively better signal-to-noise ratio, is especially suitable for such measurements. To do this, an explicit solution for the 1D heat-conduction equation of a rod- or filament-like specimen is needed.

On tunneling spectroscopy, remarkably results have been obtained on individual SWNTs, such as chirality related gap structure, one-electron tunneling, Luttinger liquid behavior, etc. However, no systematic measurement has been performed on MWNTs by now. MWNTs have diameters of several tens of nm. This is one order of magnitude higher than that of SWNTs and relates into an order of magnitude difference in energy scale. In zone-folding picture, MWNTs may still be treated as 1D conductor, then an interesting and important problem is whether or not electron correlations exist in MWNTs. Taking advantage of the very long aligned MWNTs, we can use true four-probe configuration to measure the tunneling spectroscopy on a thin bundle sample containing only several tens of nanotubes. Important information will be obtained on the possible effects of electron correlations and their relations with tube diameter.

Finally, electrical transport properties such as thermoelectric power, magnetoresistance will be investigated. For thermoelectric power measurement, the continuity of the sample guarantees the reliability of the results. For magnetoresistance measurement, the larger transverse size of MWNTs compared with SWNTs make them more suitable to explore the orbital effects. A magnetic field of 3T is enough to induce a magnetic field flux of $h/2e$ in a MWNT with outer diameter 30nm. It will be interesting to perform magnetotransport experiments of MWNTs in parallel and perpendicular field at low temperatures to explore quantum transport phenomena.

Bibliography

- [1] H. W. Kroto, J. R. Heath, S. C. O'Brien, R. F. Curl, and R. E. Smalley. C₆₀: Buckminsterfullerene. *Nature*, 318:162, 1985.
- [2] S. Iijima. Helical microtubules of graphitic carbon. *Nature*, 354:56, 1991.
- [3] S. Iijima and T. Ichihashi. Single-shell carbon nanotubes of 1-nm diameter. *Nature*, 363:603, 1993.
- [4] D. S. Bethune, C. H. Klang, M. S. de Vries, G. Gorman, R. Savoy, J. Vazquez, and R. Beyers. Cobalt-catalysed growth of carbon nanotubes with single-atomic-layer walls. *Nature*, 363:605, 1993.
- [5] A. Thess, R. Lee, P. Nikolaev, H. Dai, P. Petit, J. Robert, C. Xu, Y. H. Lee, S. G. Kim, A. G. Rinzler, G. E. Scuseria, D. T. Colbert, D. Tomanek, J. E. Fischer, and R. E. Smalley. Crystalline ropes of metallic carbon nanotubes. *Science*, 273:483, 1996.
- [6] M. S. Dresselhaus, G. Dresselhaus, and P. C. Eklund. *Science of Fullerenes and Carbon Nanotubes*. Academic Press, New York, 1996.
- [7] N. Hamada, S. Sawada, and A. Oshiyama. New one-dimensional conductors: Graphitic microtubules. *Phys. Rev. Lett.*, 68:1579, 1992.
- [8] J. W. Mintmire, B. I. Dunlap, and C. T. White. Are fullerene tubules metallic? *Phys. Rev. Lett.*, 68:631, 1992.
- [9] J. W. Mintmire and C. T. White. Electronic and structural-properties of carbon nanotubes. *Carbon*, 33:893, 1995.
- [10] R. Saito, M. Fujita, G. Dresselhaus, and M. S. Dresselhaus. Electronic structure of chiral graphene tubules. *Appl. Phys. Lett.*, 60:2204, 1992.

-
- [11] R. Saito, G. Dresselhaus, and M. S. Dresselhaus. Topological defects in large fullerenes. *Chem. Phys. Lett.*, 195:537, 1992.
- [12] P. R. Wallace. The band theory of graphite. *Phys. Rev.*, 71:622, 1947.
- [13] P. Kim, T. W. Odom, J. Huang, and C. M. Lieber. Electronic density of states of atomically resolved single-walled carbon nanotubes: Van Hove singularities and end states. *Phys. Rev. Lett.*, 82:1225, 1998.
- [14] C. L. Kane and E. J. Mele. Size, shape and low energy electronic structure of carbon nanotubes. *Phys. Rev. Lett.*, 78:1932, 1997.
- [15] L. Balents and M. P. A. Fisher. Correlation effects in carbon nanotubes. *Phys. Rev. B*, 55:R11973, 1997.
- [16] J. W. Mintmire and C. T. White. First-principles band structures of armchair nanotubes. *Appl. Phys. A*, 67:65, 1998.
- [17] J. C. Charlier and J. P. Michenaud. Energetics of multilayered carbon tubules. *Phys. Rev. Lett.*, 70:1858, 1993.
- [18] R. Saito, G. Dresselhaus, and M. S. Dresselhaus. Electronic structure of double-layer graphene tubules. *J. Appl. Phys.*, 73:494, 1993.
- [19] Ph. Lambin, L. Philippe, J. C. Charlier, and J. P. Michenaud. Electronic band structure of multilayered carbon tubules. *Computational Mater. Sci.*, 2:350, 1994.
- [20] L. X. Benedict, V. H. Crespi, S. G. Louie, and M. Cohen. Static conductivity and superconductivity of carbon nanotubes: Relations between tubes and sheets. *Phys. Rev. B*, 52:14935, 1995.
- [21] M. R. Pederson and J. Q. Broughton. Nanocapillarity in fullerene tubules. *Phys. Rev. Lett.*, 69:2689, 1992.
- [22] E. G. Gal'pern, I. V. Stankevich, A. L. Chistykov, and L. A. Chernozatonskii. Carbon nanotubes with metal inside: electron structure of tubelenes $[\text{Li}@\text{C}_{24}]_n$ and $[\text{K}@\text{C}_{36}]_n$. *Chem. Phys. Lett.*, 214:345, 1993.
- [23] J. Breton, J. Gonzalez-Platas, and C. Girardet. Endohedral adsorption in graphitic nanotubules. *J. Chem. Phys.*, 101:3334, 1994.

-
- [24] L. Langer, V. Bayot, E. Grivei, J.-P. Issi, J. P. Heremans, C. H. Olk, L. Stockman, C. Van Haesendonck, and Y. Bruynseraede. Quantum transport in a multiwalled carbon nanotube. *Phys. Rev. Lett.*, 76:479, 1996.
- [25] T. W. Ebbesen, H. J. Lezec, H. Hiura, J. W. Bennett, H. F. Ghaemi, and T. Thio. Electrical conductivity of individual carbon nanotubes. *Nature*, 381:678, 1996.
- [26] S. Frank, P. Poncharal, Z. L. Wang, and W. A. de Heer. Carbon nanotube quantum resistors. *Science*, 280:1744, 1998.
- [27] A. Bachtold, C. Strunk, J.-P. Salvetat, J.-M. Bonard, L. Forró, T. Nussbaumer, and C. Schönenberger. Aharonov-bohm oscillations in carbon nanotubes. *Nature*, 397:673, 1999.
- [28] S. J. Tans, M. H. Devoret, H. Dai, A. Thess, R. E. Smalley, L. J. Geerligs, and C. Dekker. Individual single-wall carbon nanotubes as quantum wires. *Nature*, 386:474, 1997.
- [29] M. Bockrath, D. H. Cobden, P. L. McEuen, N. G. Chopra, A. Zettl, A. Thess, and R. E. Smalley. Single-electron transport in ropes of carbon nanotubes. *Science*, 275:1922, 1997.
- [30] J. W. G. Wildöer, L. C. Venema, A. G. Rinzler, R. E. Smalley, and C. Dekker. Electronic structure of atomically resolved carbon nanotubes. *Nature*, 391:59, 1998.
- [31] T. W. Odom, J. Huang, P. Kim, and C. M. Lieber. Atomic structure and electronic properties of single-walled carbon nanotubes. *Nature*, 391:62, 1998.
- [32] R. Egger and A. O. Gogolin. Effective low-energy theory for correlated carbon nanotubes. *Phys. Rev. Lett.*, 79:5082, 1997.
- [33] R. Egger and A. O. Gogolin. Correlated transport and non-fermi-liquid behavior in single-wall carbon nanotubes. *Euro. Phys. Journal B*, 3:281, 1998.
- [34] C. Kane, L. Balents, and M. P. A. Fisher. Coulomb interactions and mesoscopic effects in carbon nanotubes. *Phys. Rev. Lett.*, 79:5086, 1997.
- [35] H. Yoshioka and A. A. Odintsov. Electronic properties of armchair carbon nanotubes: Bosonization approach. *Phys. Rev. Lett.*, 82:374, 1999.

-
- [36] S. J. Tans, M. H. Devoret, R. J. A. Groeneveld, and C. Dekker. Electron-electron correlations in carbon nanotubes. *Nature*, 394:761, 1998.
- [37] M. Bockrath, D. H. Cobden, J. Lu, A. G. Rinzler, R. E. Smalley, L. Balents, and P. L. McEuen. Luttinger-liquid behaviour in carbon nanotubes. *Nature*, 397:598, 1999.
- [38] M. M. J. Treacy, T. W. Ebbesen, and J. M. Gibson. Exceptionally high Young's modulus observed for individual carbon nanotubes. *Nature*, 381:678, 1996.
- [39] Z. W. Pan, S. S. Xie, L. Lu, B. H. Chang, L. F. Sun, W. Y. Zhou, G. Wang, and D. L. Zhang. Tensile tests of ropes of very long aligned multiwall carbon nanotubes. *Appl. Phys. Lett.*, 74:3152, 1999.
- [40] M. R. Falvo, G. J. Clary, R. M. Taylor, V. Chi, F. P. Brooks, S. Washburn, and R. Superfine. Bending and buckling of carbon nanotubes under large strain. *Nature*, 389:582, 1997.
- [41] T. W. Ebbesen, editor. *Carbon Nanotubes: Preparation and Properties*. CRC Press, 1997.
- [42] Z. W. Pan, S. S. Xie, B. H. Chang, C. Y. Wang, L. Lu, W. Liu, W. Y. Zhou, W. Z. Li, and L. X. Qian. Very long carbon nanotubes. *Nature*, 394:631, 1998.

Chapter 2

Sample growth and characterization

2.1 Introduction

For the first time, millimeter-long aligned multiwall carbon nanotubes were synthesized using thermal decomposition method by Dr. Z. W. Pan in Prof. S. S. Xie's research group [1]. Here a brief introduction of the sample growth and characterization is presented to let the readers have a first impression on the structure and morphology of MWNTs studied in this dissertation. All the materials in this chapter were kindly provided by Prof. S. S. Xie.

2.2 Process of synthesis

The method used is similar to that reported by W. Z. Li et al. [2], but some improvement has been made in substrate preparation. Instead of using bulk mesoporous silica containing iron nanoparticles embedded in the pores as substrate, silica film on the surface of which iron/silica nanocomposite particles are evenly positioned was utilized. The iron/silica substrate was prepared by a sol-gel process using the technique described in Ref. [1]. Tetraethoxysilane (10 ml) was mixed with 1.5 M iron nitrate aqueous solution (15 ml) and ethanol (10 ml) by magnetic stirring for 20 min. A few drops of concentrated hydrogen fluoride (0.4 ml) was then added, and the mixture was stirred for another 20 min. The mixture was then dropped onto a quartz plate to form a film of thickness 30–50 μm . After

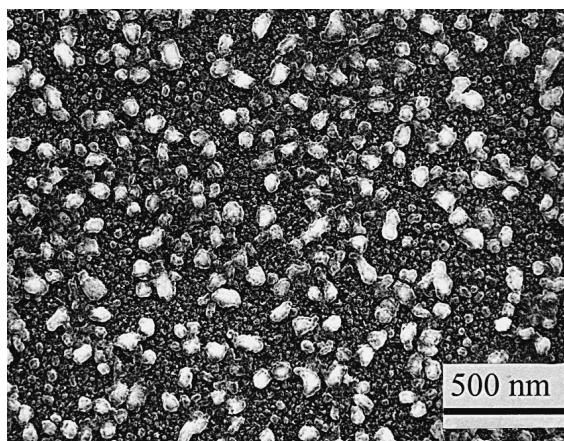


Figure 2.1: SEM image of the iron/silica substrate after reduction, showing iron/silica nanocomposite particles with size of 5–50 nm present evenly on every surface of the substrate.

gelation of the mixture, the gel was dried overnight at 80°C to remove the excess water and other solvent, during which the gel cracked into small pieces of substrates of area 5–20 mm².

The substrates were placed in a quartz boat and were then introduced into a chamber of a tube furnace. The substrate were calcined at 450°C for 10 h under vacuum ($< 10^{-3}$ Torr) and then reduced at 500°C for 5 h in a flow of 9% hydrogen in nitrogen under 180 Torr. At this stage, large quantities of nanoparticles with size of 5–50 nm formed evenly on all surfaces of the substrates (Fig. 2.1). Energy-dispersive X-ray (EDX) spectra taken from these nanoparticles showed the presence of iron, silicon and oxygen (68.7, 14.5 and 16.8 wt%, respectively), which indicated that these nanoparticles were iron/silica nanocomposite particles. The iron/silica particles were believed to act as catalysts for nanotube growth. Subsequently, a flow of 9% acetylene in nitrogen was introduced into the chamber at a flow rate of 110 cm³/min, and carbon nanotubes were formed on the substrate by deposition of carbon atoms from decomposition of acetylene at 600°C under 180 Torr (Fig. 2.2). The growth time varied from 1 to 48 h.

The as-grown nanotubes were examined by a scanning electron microscope (SEM; S-4200, Hitachi), and EDX spectra were recorded by a SiLi detector attached to the SEM. A transmission electron microscope (TEM; JEOL JEM-200cx at 200 keV) was used to characterize the fine structures of nanotubes.

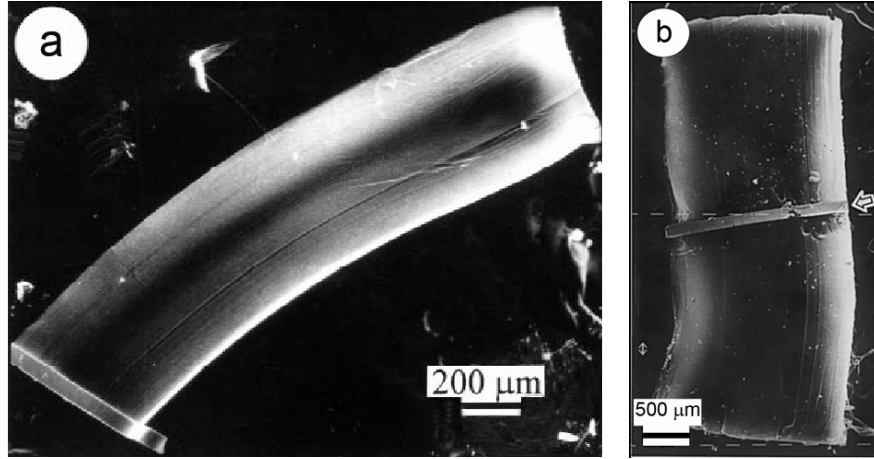


Figure 2.2: Low-magnification SEM images of a sample after 48 hours of growth. (a) Only one nanotube array remains after stripping off other arrays from the other sides of the substrate. (b) Two nanotube arrays grown from the upper and lower sides of the substrate. From Ref. [1]

2.3 Characterization

SEM and TEM

High-magnification SEM image (Fig. 2.3a) shows that carbon nanotubes grow out separately and perpendicularly from the substrate to form an array. The nanotubes within the array are of uniform external diameter (20–40 nm) and spacing (~ 100 nm) between tubes (Fig. 2.3b). Most of the nanotubes in the array are highly aligned, although a few of them appear to be slightly tangled or curved. We note that no traces of polyhedral particles or other graphitic nanostructures are detected in both the bottom part and central part of the array, which indicates that the nanotubes prepared in this study have very high purity and thus have very high quality.

The nanotube array can be easily stripped off from the substrate without destroying the array's integrity, and the SEM images taken from the bottom end of the array confirm that the nanotubes are highly aligned and well separated (Fig. 2.3c, d). EDX spectra collected from the bottom end of the array demonstrate the presence of carbon alone, neither silicon nor iron could be detected.

Low-resolution TEM observations of the bottom end of the nanotube array reveal that no seamless caps exist at the bottom ends of the nanotubes and the tubes are indeed

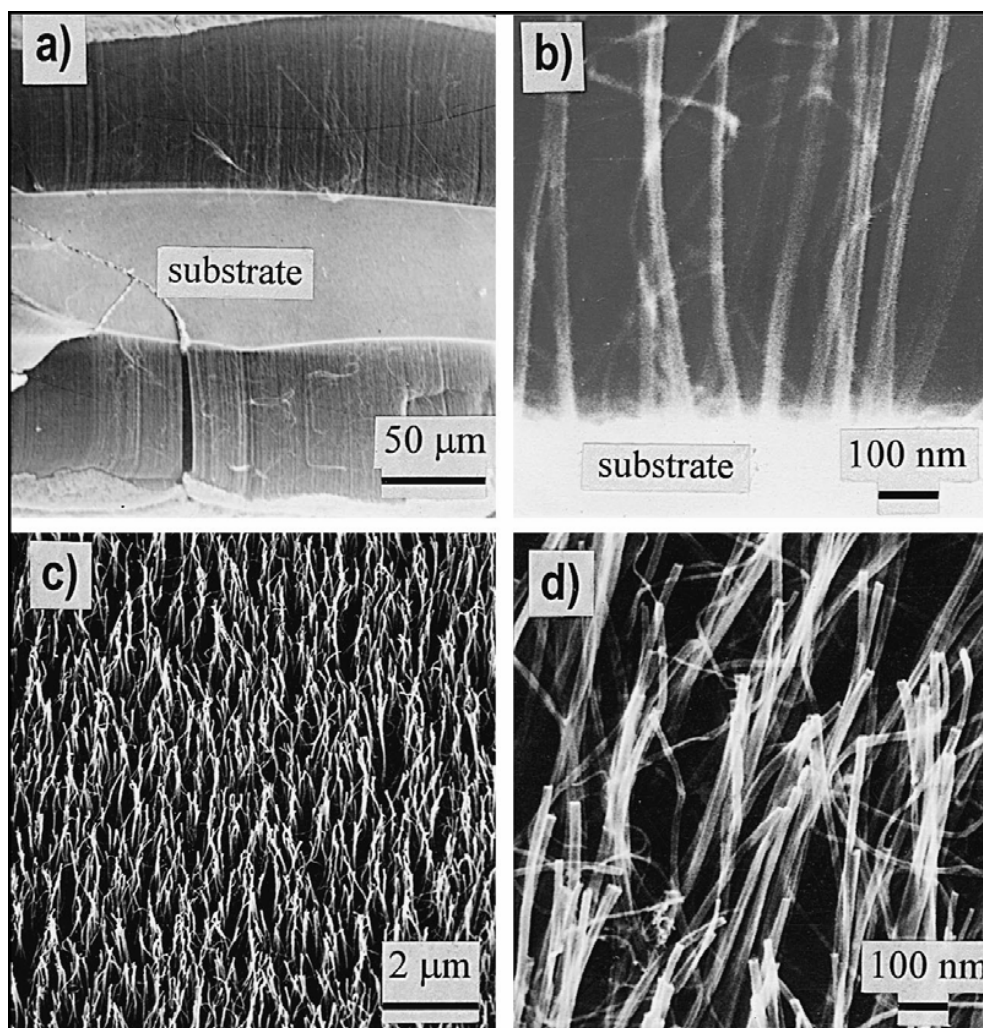


Figure 2.3: High-magnification SEM images of aligned carbon nanotube arrays. (a) Aligned nanotubes grow outwards perpendicularly from the surface of the substrate to form nanotube arrays. (b) Higher magnification of the nanotube array showing aligned nanotubes have uniform external diameters (20–40 nm) and spacing (~ 100 nm) between tubes. (c, d) Bottom structure of the nanotube array showing well-separated, aligned and open nanotubes. From Ref. [3]

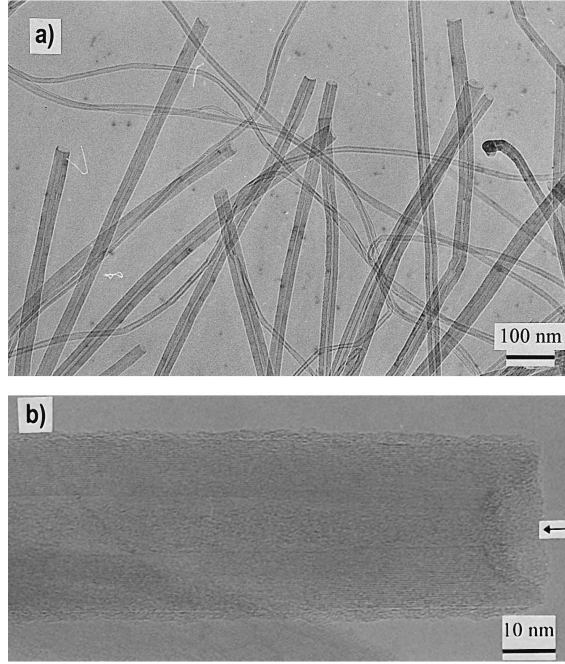


Figure 2.4: (a) Low-resolution TEM image of the bottom end of the nanotube array showing aligned open carbon nanotubes. Encapsulated iron/silica nanocomposite particles are absent. (b) High-resolution TEM image of the bottom end of an open nanotube showing bowl-shape structure (see arrow) formed by the graphite sheets. From Ref. [3]

opened (Fig. 2.4). The inner and outer diameters of the open nanotubes are 10–15 and 20–40 nm, respectively. Encapsulated particles are not observed at the bottom ends of the nanotubes. High-resolution TEM observations confirm that the nanotubes are opened at the bottom ends. The nanotubes are well graphitized and typically consist of 10–30 concentric graphite layers.

Raman spectroscopy

Raman spectroscopy is a very useful tool to characterize carbon materials because it gives information on the hybridization (sp^n) state, the size of the graphite crystallites and the degree of ordering of the material. Crystalline graphite, such as highly oriented pyrolytic graphite (HOPG), belongs to the space group D_{6h}^4 with the vibrational modes having the irreducible representation $\Gamma = 2E_{2g} + E_u + A_{2u} + 2B_{2g}$. Only the two E_{2g} modes are Raman active. These correspond to the movement of two neighbouring carbon atoms in a graphene sheet. HOPG is characterized by a single strong band at 1580 cm^{-1} which is one of these

E_{2g} modes. On the other hand, glassy carbon has its most intense band at approximately 1350 cm^{-1} which is normally explained by the relaxation of the wave vector selection rule due to the finite size of the crystallites in the material.

For raw MWNTs made by the arc-discharge method, the first-order Raman spectra has a weak and broad peak at 1346 cm^{-1} (D band) and a strong peak at 1574 cm^{-1} (G band) [4]. The G band is very similar to 1580 cm^{-1} G band of HOPG but is slightly downshifted perhaps due to the curvature in the carbon network. The width of this peak is almost same to that of HOPG (approximately 23 cm^{-1}), suggesting a highly crystalline graphitic structure. The 1346 cm^{-1} peak is a disorder-induced peak in graphitic structures and in nanotubes it could arise from the smaller crystallite sizes, defects in the curved graphene sheets or at the tube ends. Considering the Raman features, MWNTs must be seen as graphite-like microcrystals and are unlike fullerenes which show vibrational features of molecules.

Z. W. Pan et al. studied micro-Raman spectroscopy of arrays of high-density aligned MWNTs made by thermal decomposition method and compared their results with that of HOPG and MWNTs made by arc-discharge method [5]. Here is a brief description of their results.

Raman scattering experiments were performed at ambient conditions by a micro-Raman spectrometer (Reinshaw, England) in a backscattering geometry. The spectra were collected by using 514.5 nm excitation of argon laser at 0.2 mW and a spectral slitwidth $\leq 2\text{ cm}^{-1}$, with the laser incident perpendicular to the orientation of nanotube arrays. The diameter of focus area of laser beam is about $2\text{ }\mu\text{m}$. The time for collecting every spectrum is $5\text{ s} \times 3$.

Shown in Fig. 2.5 are Raman spectra of aligned MWNTs. Fig. 2.5a are first-order and second-order Raman spectra, Fig. 2.5b is third-order Raman spectrum. No smoothing was applied to the spectra. In Fig. 2.5a, the 1570 cm^{-1} peak (G band) is the high-frequency Raman active E_{2g} mode. It is downshifted by 11 cm^{-1} compared with G band (1581 cm^{-1}) of HOPG, but is close to G band (1574 cm^{-1}) of MWNTs made by arc-discharge method. Remarkably, a strong peak can be seen at 1320 cm^{-1} (D band), and a weak peak at 1598 cm^{-1} (D' band) appears. It is noticeable that the strong 1320 cm^{-1} peak resembles the D band of pyrolytic graphite (PG), but can not be observed in HOPG. In other carbon materials, the appearance of D and D' band is attributed to the crystallite-size effect or lattice twisting. The ratio of intensity of D band relative to G band reflects the size of

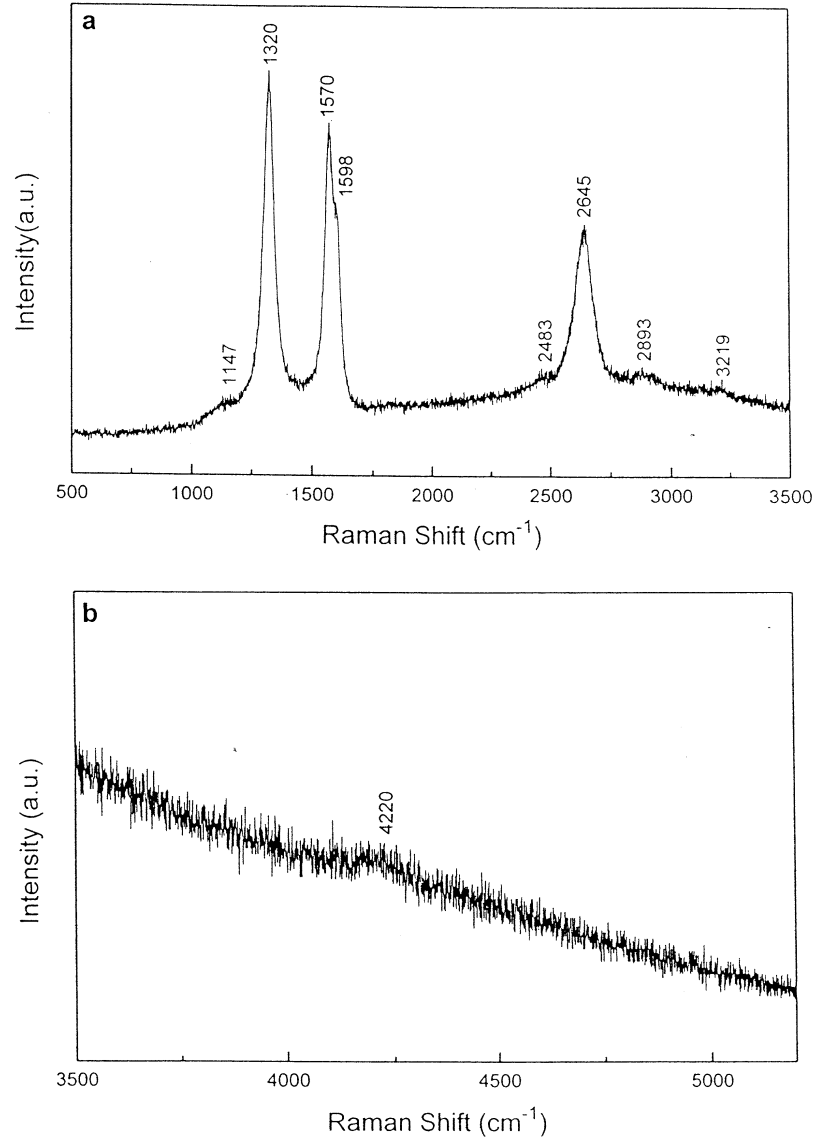


Figure 2.5: Micro-Raman spectra of aligned multiwall carbon nanotubes. (a) first-order and second-order Raman spectra. (b) Third-order Raman spectrum. From Ref. [5]

graphitized crystallites. In SEM and TEM studies, no carbon nano-particles was found. Therefore, the appearance of 1320 cm^{-1} peak could be attributed to defects in the curved graphene sheets or at the tube ends, turbostratic structure in graphene sheets, limited size of crystal domains in nanotubes and the coating of amorphous carbon at nanotube surfaces. Compared with MWNTs made by arc-discharge method, the intensity of D band is much higher. This mainly due to the much lower growth temperature of pyrolysis method (600°C). The results of Raman spectroscopy show that MWNTs made by pyrolysis method have relatively lower degrees of graphitization and larger amounts of defects.

In the second-order Raman spectrum, four peaks at 2645 cm^{-1} , 2893 cm^{-1} , 2483 cm^{-1} and 3219 cm^{-1} can be seen. The 2645 cm^{-1} band is the second-order spectrum of D band ($\sim 2 \times 1320\text{ cm}^{-1}$), the 2893 cm^{-1} band is identified as composition of D band and G band ($1320\text{ cm}^{-1} + 1570\text{ cm}^{-1}$).

In the third-order Raman spectrum, a weak 4220 cm^{-1} peak can be recognized. This peak is the third-order Raman spectrum of nanotubes and can be identified as composition of D band and G band ($2 \times 1320\text{ cm}^{-1} + 1570\text{ cm}^{-1}$). It is downshifted compared with 4320 cm^{-1} peak of HOPG and 4305 cm^{-1} peak of PG. No fourth-order Raman spectrum was observed in this experiment.

From the above analysis, the Raman feature of MWNTs prepared has a strong resemblance to that of PG. This indicates that many nanometer-sized crystal domains exist in microscopic structure of MWNTs. The appearance of the third-order Raman spectrum shows that these crystal domains have high degrees of crystallization, which agrees with the conclusion from TEM studies.

2.4 Summary

Aligned and open-ended multiwall carbon nanotubes (MWNTs) were prepared by Dr. Z. W. Pan at a very high yield by pyrolysis of acetylene over film-like iron/silica substrates. These nanotubes grow outwards separately and perpendicularly from the surfaces of the substrates to form aligned nanotube arrays. The nanotubes within the arrays are of uniform outer diameters (20–40 nm), with a spacing of $\sim 100\text{ nm}$ between the tubes. After continuous growth of 48 hours, the lengths of nanotubes can reach 2–3 mm, which is 1–2 orders higher than previously reported values. TEM studies indicate a high degree of graphitization. The multiwall nanotubes are composed of 5–30 concentric graphene cylin-

ders with average inter-wall distance of 0.34 nm. The inner diameters of nanotubes are 3–10 nm. Features of micro-Raman spectra show a strong resemblance to that of Pyrolytic Graphite. The appearance of a strong D band indicates the existence of nanometer-sized crystal domains in MWNTs. The appearance of the third-order Raman spectrum shows that MWNTs have high degrees of crystallization.

Bibliography

- [1] Z. W. Pan, S. S. Xie, B. H. Chang, C. Y. Wang, L. Lu, W. Liu, W. Y. Zhou, W. Z. Li, and L. X. Qian. Very long carbon nanotubes. *Nature*, 394:631, 1998.
- [2] W. Z. Li, S. S. Xie, L. X. Qian, B. H. Chang, B. S. Zou, W. Y. Zhou, R. A. Zhao, and G. Wang. Large-scale synthesis of aligned carbon nanotubes. *Science*, 274:1701, 1996.
- [3] Z. W. Pan, S. S. Xie, B. H. Chang, L. F. Sun, W. Y. Zhou, and G. Wang. Direct growth of aligned open carbon nanotubes by chemical vapor deposition. *Chem. Phys. Lett.*, 299:97, 1999.
- [4] H. Hiura, T. W. Ebbesen, K. Tanigaki, and H. Takahashi. Raman studies of carbon nanotubes. *Chem. Phys. Lett.*, 202:509, 1993.
- [5] Z. W. Pan. unpublished data.

Chapter 3

Thermal properties

3.1 Introduction

While the electronic properties of carbon nanotubes have been intensively studied and shown to be peculiar, such as the sensitive dependence of the electronic structure on the diameter and chirality of the tubule, the thermal properties of the material are not well characterized experimentally, though they are as important as the former both from the viewpoint of basic research and for possible application. Benedict *et al.* [1] predicted that the temperature dependence of specific heat would depend on the diameter of the tubule, and might even show a sign of dimensional cross-over as the temperature is varied. However, an experimental test of the thermal properties of the material is frustrated because the samples usually available are in a mat-like form, in which each individual tubule, or rope of tubes, is rather short and only loosely connected to each other, which prevents a reliable and equilibrium thermal measurement. The recent success in synthesis of millimeter-long highly aligned array of MWNTs [2] enables us to perform specific heat and thermal conductivity measurements on well-defined samples.

3.2 Experimental

The MWNTs were synthesized through chemical vapor deposition (CVD) [2]. High magnification scanning electron microscopy (SEM) analysis shows that the tubules grow out perpendicularly from the substrate and are evenly spaced at an averaged inter-tubule distance of ~ 100 nm, forming a highly aligned array. High resolution transmission electron

microscopy (HRTEM) study shows that most of the tubules are within a diameter range of 20–40 nm. The mean external diameter is ~ 30 nm. A tubule may contain 10–30 walls, depending on its external diameter. The continuity of the tubules, which is of crucial importance for the interpretation of the thermal conductivity data, is indicated by SEM studies, and by Young's modulus measurement where several tenth of TPa, a value higher than that of steel, was reached [3]. The final samples used in our measurements were 1–2 mm long bundles of MWNTs stripped off from the bulk array. The apparent cross-section of the samples spreads from 10^{-10} to 10^{-8} m². The filling factor of MWNTs in the bundles is $\sim 1.5\%$, estimated from SEM observation. This estimation may bring some uncertainty in determining the absolute values of the thermal conductivity and specific heat of the MWNTs. However, their temperature dependence is not affected by this uncertainty.

Measurements of thermal conductivity and specific heat on such tiny but well defined samples were made possible by using a self-heating 3ω method. The basic idea of the method can be traced back to 1910 [4], and was carefully tested later on. If both voltage contacts of the sample are ideally heat sunk to the substrate, but keeping the in-between part suspended (illustrated in Fig. 3.1), an *ac* current of the form $I_0 \sin \omega t$ passing through the sample will create a temperature fluctuation at 2ω , which will further cause 3ω voltage harmonics, $V_{3\omega}$, across the voltage contacts. $V_{3\omega}$ can be solved explicitly to an accuracy of $\sim 1/81$ [5]:

$$V_{3\omega} = \frac{2I_0^3 LR (dR/dT)}{\pi^4 \kappa S \sqrt{1 + (2\omega\gamma)^2}} \sin(3\omega t - \phi_0) \quad (3.1)$$

$$\tan \phi_0 = 2\omega\gamma \quad (3.2)$$

where $\gamma = L^2/\pi^2 a^2$, $a^2 = \kappa/C_p \rho_m$ is the diffusivity coefficient, κ , the thermal conductivity, C_p , the specific heat, ρ_m , the density, R , the resistance, L , the length (between voltage contacts), and S , the cross-section of the sample. By measuring the frequency dependencies of the amplitude and the phase shift ϕ_0 of $V_{3\omega}$ in proper ω and I_0 ranges (typical results are shown in Fig. 3.1), both κ , a^2 , and hence C_p of the sample can be determined. This method was verified to be reliable on pure Pt-wire samples. The measured C_p of Pt agrees with the standard data within an accuracy of 5% from 10 K to 300 K.

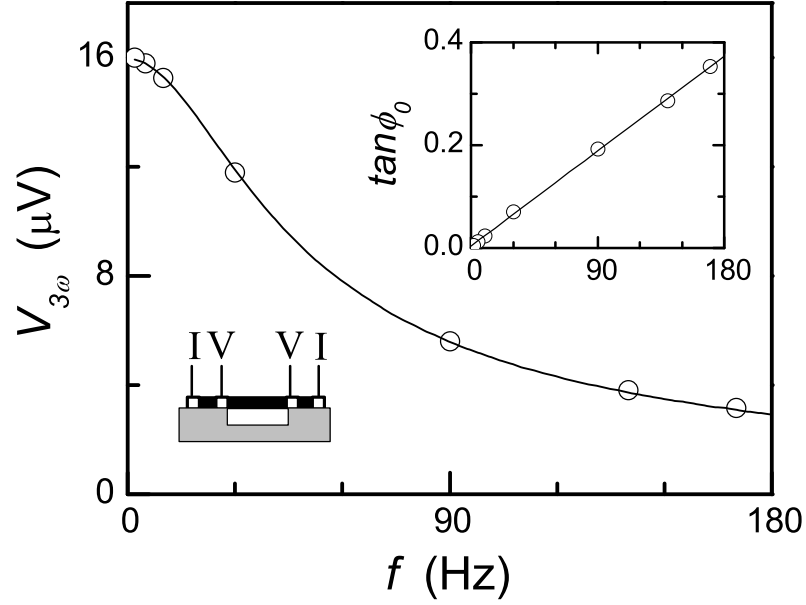


Figure 3.1: The frequency dependence of the amplitude (main frame) and the phase shift ϕ_0 (upper right inset) of the 3ω voltage measured on one of the samples at $T = 50$ K. Solid lines are the predictions of Eqs. 1 and 2. Lower left inset: schematic diagram of sample mounting. The samples were glued to sapphire substrate with silver paint in such a way that the inner part between two voltage contacts was suspended. The silver paint contacts serve both as electrodes and heat sinkers of the sample. The 3ω voltage was measured by using a lock-in amplifier (SR850). The whole set-up was heat-shielded to the substrate temperature and was maintained in high vacuum, to preclude heat leakage through air. The total heating power at each measured temperature was adjusted to be small comparing to the value of sample's thermal conductance. The heat leakage through radiation is estimated to be less than 5%.

3.3 Results and discussion

Shown in Fig. 3.2 are the main results. First we notice that, while both κ and a^2 are significantly non-linear, C_p calculated from them follows a pretty linear T -dependence over the entire temperature range measured. We note that a T -linear phonon specific heat was predicted for some special systems, but seldom observed experimentally over such a wide temperature range. This behavior is dominated by the phonon contribution, since the electron contribution is negligible in the temperature range of this experiment, as expected from the fact that the electron density of states is either very low or gapped at the Fermi surface of carbon nanotubes [6–8].

The phonon contribution can generally be written as:

$$C_p = \int_0^{\omega_{max}} k_B \left(\frac{\hbar\omega}{k_B T} \right)^2 \frac{e^{\frac{\hbar\omega}{k_B T}} \rho(\omega) d\omega}{(e^{\frac{\hbar\omega}{k_B T}} - 1)^2} \quad (3.3)$$

where $\rho(\omega)$ is the phonon spectrum determined by the phonon energy dispersion $\omega(k)$ of different modes, and by the occupational dimensionality of phonon excitations in k -space. Detailed explanation of the T -dependence of C_p requires the information on the $\rho(\omega)$ of the MWNTs. While the $\rho(\omega)$ and $\omega(k)$ for single-wall tubules of ~ 1 nm diameter have been calculated numerically and shown to have a linear phonon dispersion and 1D behavior [10–12], such calculation is virtually impossible to be performed on tubules of a few tens nm diameters, containing over hundreds of hexagonal cells along the circumference. Nevertheless, one can still find immediately from Eq. 3.3 that a constant $\rho(\omega)$ would result in a linear T -dependence of C_p when $T \ll \Theta_D = \hbar\omega_{max}/k_B$, the Debye temperature. This condition is believed to hold in our case, referring to the fact that the C–C bond configuration within the wall is pretty much the same as in graphite, hence its Θ_D should not be far from ~ 2400 K [9]. Therefore, we conclude that the linear T -dependence of C_p represents a constant $\rho(\omega)$ of the MWNTs for the phonon states excitable in the temperature range of this experiment. It is less likely that a complicated $\rho(\omega)$ could “happen” to result in a linear C_p after the integration, in this case one would usually get a complicated T -dependence of C_p . Strictly speaking, due to the rolled-up nature of the material, there should exist some spiky-like structures over the flat background of MWNTs’ $\rho(\omega)$. Such structure is most significantly seen in tubules with smallest diameter [11]. Nevertheless, thermal properties like C_p are integration over a wide frequency range and hence would be rather insensitive to the local spiky structures.

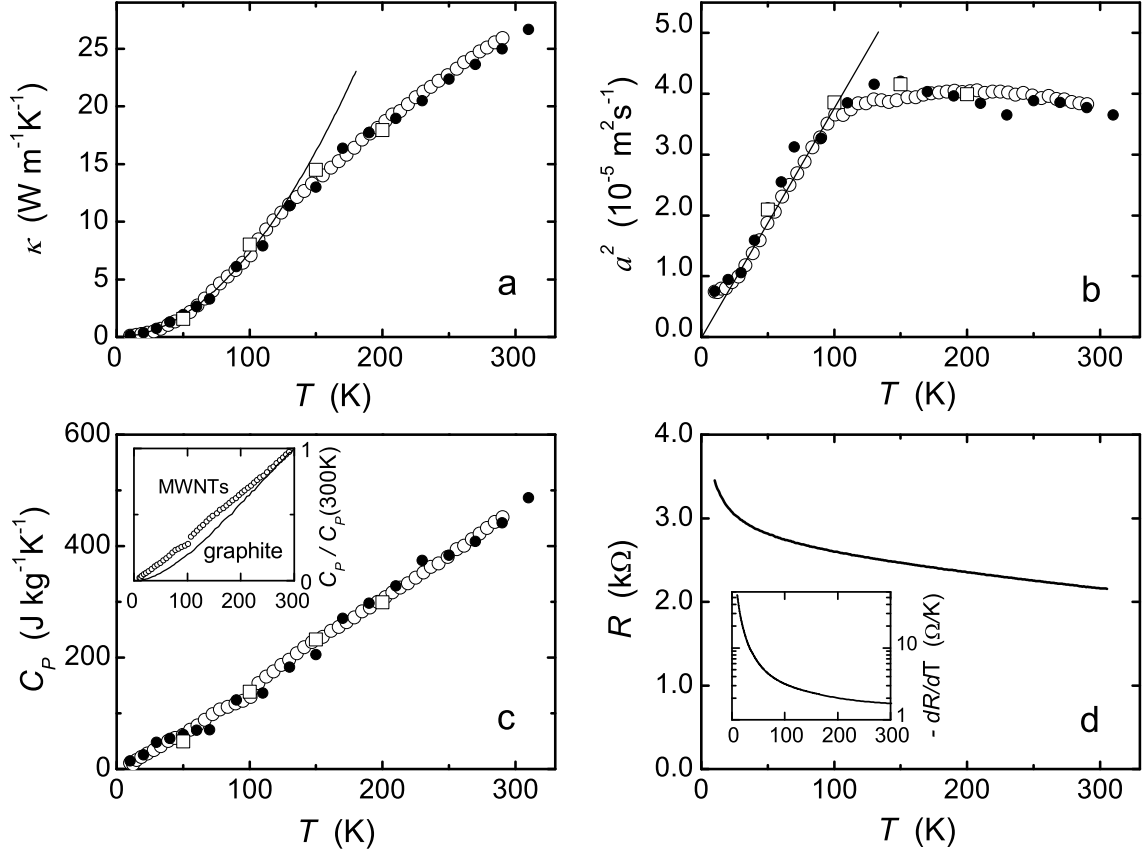


Figure 3.2: (a) Temperature dependence of the thermal conductivity of three MWNT samples. It is roughly linear above ~ 120 K, but becomes quadratic at temperatures below: $\kappa \propto T^{1.98 \pm 0.03}$ (the solid line). (b) The thermal diffusivity coefficient of the samples. (c) The specific heat of the samples, calculated using the data in figures (a) and (b), showing a linear temperature dependence, which differs significantly from that of graphite [9] (see the inset). For graphite, $C_p(300K) \simeq 720$ Wm⁻¹K⁻¹. (d) Typical resistance R (main frame) and dR/dT (inset) of the samples, which are used by Eq. 3.1 to calculate the κ and a^2 .

A constant $\rho(\omega)$ usually originates from linearly dispersed branches in a 1D system, or from one or more quadratically dispersed branches in a 2D system. The dimensionality of our MWNTs can be determined through the following criteria [1]. Because of the rolled up structure, the allowable phonon states are quantized in k -space, forming some discrete lines parallel to the tubule axis. A tubule is strictly 1D-like if only those states on the central line are thermally excitable, otherwise if many lines are occupied with phonons then the tubule should be 2D-like. A simple estimation shows that even at the lowest temperature of this experiment (~ 10 K), and even for the inner-most wall of our MWNTs (which has the largest inter-line distance), the thermally excitable phonon states would cover several to several tens of lines, depending on whether a linear or a quadratic dispersion is assumed. Therefore, our MWNT at higher temperatures (*i.e.*, ≥ 10 K) can approximately be regarded as a 2D system with a constant $\rho(\omega)$. This approximation sounds better if considering the fact that the outer walls, which have larger weight on the total C_p than the inner walls, undergo dimensional cross-over at even lower temperatures.

Such a phonon structure is similar to, but still different from that of graphite whose $\rho(\omega)$ is only roughly flat in a moderate frequency range [13]. The similarity is easy to understand, for that graphite is the parent material of MWNTs. The central issue now is how to understand the difference in $\rho(\omega)$ induced by the rolling up of graphene sheets. For flat sheet, as in graphite, its hexagonal symmetry leads to a quadratically dispersed acoustic phonon branch, corresponding to the out-of-plane vibration mode of the sheet. This branch contributes to a constant term in $\rho(\omega)$ [13–16] (Fig. 3.3). However, there are at least two reasons that prevent graphite from strictly demonstrating a constant $\rho(\omega)$ and a linear C_p . First, inter-layer coupling could not be neglected at low frequencies, which gives $\rho(\omega) \sim \omega$ and $C_p \sim T^2$ (in the temperature range of interest here we do not consider the case of very low frequencies). Second, the other two linearly dispersed in-plane branches, which gives $\rho(\omega) \sim \omega$ and $C_p \sim T^2$, also contribute to the total specific heat [14, 15]. Therefore, no strictly T -linear C_p as well as strictly flat $\rho(\omega)$ exist [9].

From the above discussion, the fact that MWNTs' linear $C_p(T)$ extrapolates to the (0, 0) point seems to indicate that the out-of-plane acoustic mode (as in a graphene sheet) dominates the thermal properties of this 2D-like material, and that the two in-plane acoustic modes, presumably linearly dispersed, give a negligible contribution. Here an assumption has spontaneously been made: for MWNT of a few tens nm diameter its acoustic phonon modes can still be classified as one LA and two TAs as in graphite. This assumption should

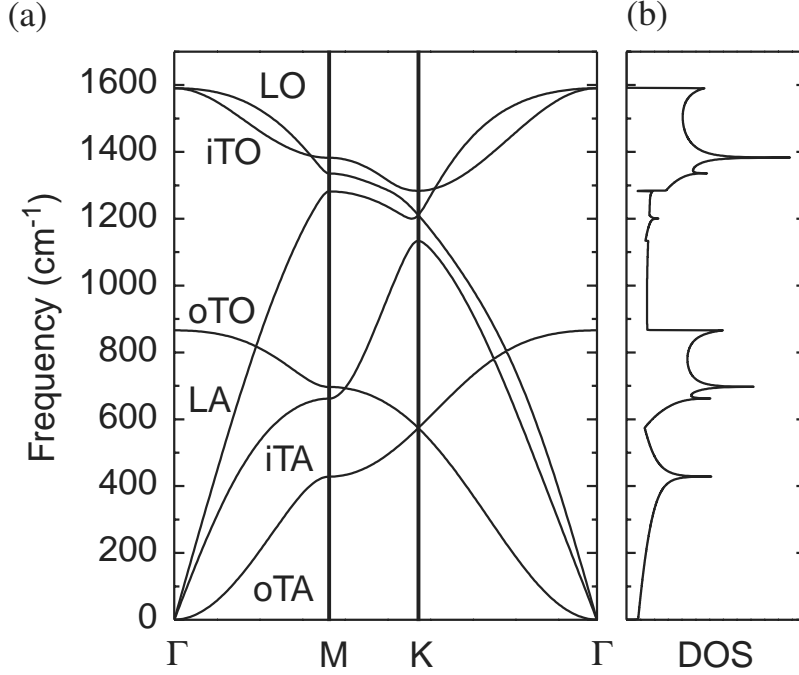


Figure 3.3: Graphite phonon dispersion relations and the corresponding phonon density of states. From Ref. [17]

be true, for that at most temperatures of this experiment the wavelengths of the majority of phonons are much shorter than tubules' diameter, *i.e.*, many lines in k -space are occupied with phonons. The striking linearity of C_p further indicates that the coupling between the walls in MWNTs is much weaker than that in graphite, so that one can treat a MWNT as a few decoupled single-wall tubules, as far as their vibrational properties are concerned.

Two facts may be responsible for the weak inter-wall coupling: the larger inter-wall distance in MWNT than the inter-layer distance in graphite, and the turbostratic stacking of adjacent walls which is unavoidable in the rolled-up structures. Although there are a number of experiments indicating that the inter-wall distance in MWNT is larger than that in graphite [18,19], recent HRTEM study [20] shows that the inter-wall distance decreases as tubule's diameter increases, at diameters ≥ 10 nm it saturates to ~ 0.344 nm, a characteristic inter-layer distance in turbostratic stacking. Therefore, we believe that the weak inter-wall coupling in MWNT is rather caused by the turbostratic stacking of adjacent walls.

The thermal conductivity of our MWNTs is rather low compared to what is generally expected [21]. Since the apparent Wiedemann-Franz ratio $R(\kappa S/L)/T$ is about two orders of magnitude larger than the free electron Lorenz number, the measured κ

essentially reflects the phonons contribution, similar to the cases in graphite and carbon fibers. Whereas κ of graphite shows a marked maximum around 100 K, κ of our MWNTs monotonously decreases with lowering temperature. If roughly expressing κ as $\kappa \sim T^n$, then n is a little less than unity above ~ 120 K, resulting in a faint hump of diffusivity a^2 between 120–300 K. Below ~ 120 K, κ follows almost a quadratic T -dependence, *i.e.*, $n \simeq 1.98$, leading to a quick decrease of a^2 , or to say, a nearly linear decrease of apparent phonon mean-free-path with temperature. This behavior indicates that drastic change in phonon scattering mechanism occurs at ~ 120 K. Comparing with graphite, although the κ of the latter also roughly takes a quadratic temperature dependence at low temperatures, the mean-free-path of phonons in graphite is rather confined by boundary scattering, because the C_p of graphite is quadratically temperature-dependent at low temperatures (*i.e.*, below 70 K [22]). An energy-dependent mean-free-path in MWNTs contradicts to the usual boundary scattering mechanism seen in graphite and other solids at low temperatures. One difference between nanotubes relative to graphite sheets is the existence of the radial breathing mode in the former [23]. Perhaps the thermal excitation of such phonons is responsible for the change in scattering mechanism around 120 K. Further investigation is needed to clarify the issue.

The MWNTs grown by CVD method at temperatures as low as ~ 600 K are far from perfect, as indicated by the fact that their thermal conductivity and electrical conductivity are about two orders of magnitude lower than those of perfect crystalline graphite at room-temperature. The average electrical resistivity of MWNTs was estimated by assuming that all walls in a MWNT conduct electric current, the characteristic value is about $1 \times 10^{-4} \Omega\text{m}$ at 300 K. This value, together with the weak negative temperature-dependent coefficient, are similar to those of disordered semimetallic graphite, and are comparable to previously reported data on MWNT bundles [25–27]. Figure 3.4 shows that the T -dependent behavior of MWNTs resembles those of not well graphitized materials such as the as-grown carbon fibers and glassy carbons [24], whose in-plane domain size of the hexagonal ordering is only a few nm. It has been shown in those materials that the mean-free-path of the phonons deduced from the κ data is well correlated with the domain size [24,28]. We therefore speculate that the domain size of our CVD-derived MWNTs is the same as the phonon mean-free-path l , which is a few nm if estimated using the classical relation $\kappa \sim C_p v l$ and assuming a characteristic sound velocity $v \sim 10^4$ m/s. This picture is further supported by micro-Raman investigation wherein the 1320 cm^{-1} band, which is prohibited in perfect

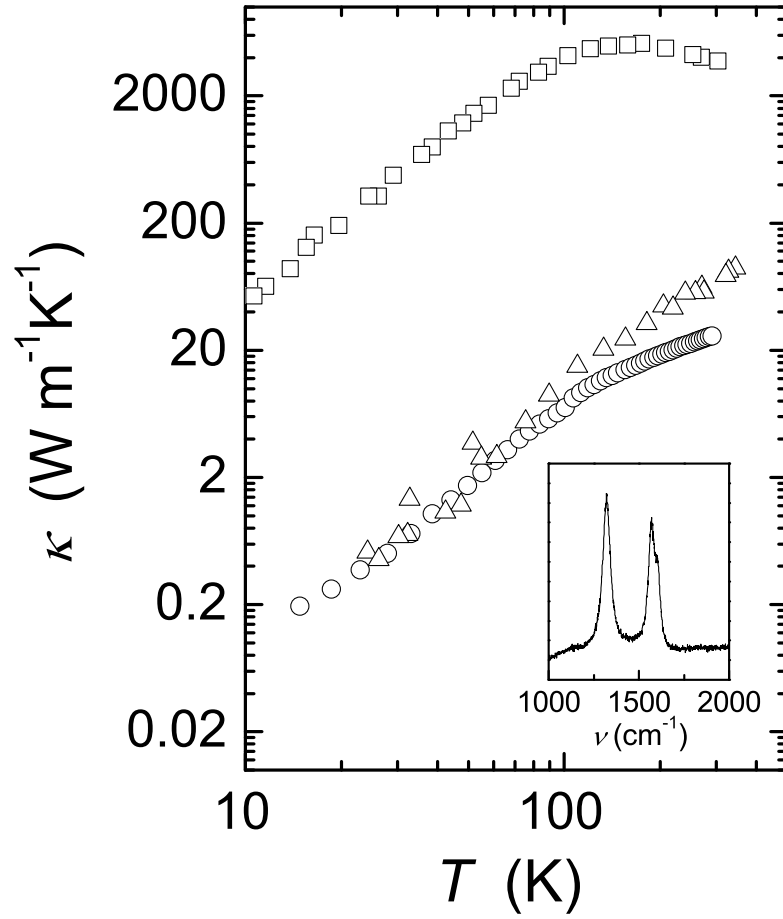


Figure 3.4: A log-log plot of the thermal conductivity of our samples (circles) comparing with that of vapor-grown carbon fibers [24] (triangles: as-grown, squares: heat treated at 3000 °C). Inset: First-order Raman spectrum of our MWNTs.

graphite, becomes substantially high in our MWNTs, resembling the case of as-grown CVD carbon fibers [24]. Nevertheless, the gross phonon spectrum is unlikely to be significantly altered upon the reduction of the domain size to a few nm [24]. We also note that for disordered systems, a two-level mechanism could contribute to a linear term of specific heat additive to the ordinary term and even surpass the latter at very low temperatures [29]. Obviously, such a mechanism, if exists, cannot account for a total linear C_p of the MWNT over the entire temperature range measured. Therefore, our previous discussions on the C_p and the phonon structure of the MWNTs should still be valid.

3.4 Summary

The specific heat and thermal conductivity of millimeter-long aligned carbon multiwall nanotubes (MWNTs) have been measured. As a rolled-up version of graphene sheets, MWNT of a few tens nm diameter is found to demonstrate a strikingly linear temperature-dependent specific heat over the entire temperature range measured (10–300 K). The results indicate that inter-wall coupling in MWNT is rather weak compared with in its parent form — graphite, so that one can treat a MWNT as a few decoupled two-dimensional (2D) single wall tubules. The thermal conductivity is found to be low, indicating the existence of substantial amount of defects in the MWNTs prepared by chemical-vapor-deposition method.

3.5 Appendix: 3Ω method

We present here a novel and simple way to measure the specific heat and thermal conductivity of rod- or filament-like specimens. This method uses four-probe configuration same as for measuring electrical resistance, except for that the voltage contacts serves not only as electrical contacts but also as thermal contacts, to heat-sink the specimen at these two points to the substrate temperature. The specimen, which needs to be electrically conductive and with a temperature-dependent resistance, serves both as heater and temperature sensor to tell the thermal response of the material. With this method we have successfully reproduced the specific heat and thermal conductivity of Pt-wire specimens, and measured the specific heat and thermal conductivity of tiny carbon nanotube bundles,

some of which are only $\sim 10^{-9}$ g in mass.

Specific heat and thermal conductivity are two of the most fundamental properties of the condensed matter. Over the past centuries, many methods have been developed for measuring these quantities. One noticeable category of the methods is the so called “ 3ω ” method, which uses a narrow-band technique in detection, and therefore gives a relatively better signal-to-noise ratio, especially for the measurement on small specimens. In this method, either the specimen itself serves as a heater and at the mean time a temperature detector, if the specimen is electrically conductive and with a temperature-dependent electrical conductivity, or, for electrically non-conductive specimens, a metal strip is artificially deposited on the surface of the specimen to serve as the heater and detector. An *ac* current of the form $I_0 \sin \omega t$ passing through the specimen or the metal strip creates a temperature fluctuation at an angular frequency of 2ω , and consequently, a resistance fluctuation at 2ω , which further generates a voltage fluctuation at 3ω . Corbino [4] is probably the first person noticed that the temperature fluctuation of an *ac* heated wire gives useful information about the thermal properties of the constituent material. Systematic investigations to the 3ω method were carried out mainly during the 1960’s [30–32], and in the recent ten years [33–38] which made this method a beautiful and practicable method. Nevertheless, we notice that in the previous works the heat-conduction equation were solved under the approximations either only for high-frequency limit [30, 31, 38], or only for low-frequency limit [33, 35, 36]. After these approximations one accordingly either loses the information of the thermal conductivity, or the specific heat of the specimen.

Here we present an explicit solution for the 1D heat-conduction equation. With this solution and together with the use of digital lock-in amplifier available nowadays, we are able to simultaneously obtain the specific heat and the thermal conductivity of a rod- or filament-like specimen through measuring the 3ω voltage using a simple four-probe configuration. We have tested this method on Pt wire specimens. Correct values of specific heat, thermal conductivity, and Wiedemann-Franz ratio, were obtained. With this method, we are able to measure the thermal properties of very tiny specimens such as carbon nanotubes, sometimes only 10^{-9} g in mass.

In Section 3.5.1 we will present an explicit solution of the heat-conduction equation. In Section 3.5.2 we will give the experimental test of the method on Pt wires (results on carbon nanotubes are already presented previously). A summary of the method will be in the last section.

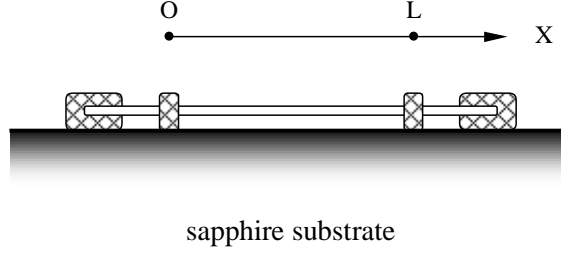


Figure 3.5: Illustration of the four-probe configuration for measuring the specific heat and thermal conductivity of a rod- or filament-like specimen.

3.5.1 Solution of the 1D heat-conduction equation in the presence of an AC heating current

We consider a uniform rod- or filament-like specimen in a four-probe measurement configuration as shown in Fig. 3.5. The two outside contacts are used to feed an *ac* current of the form $I_0 \sin \omega t$ into the specimen, and the two inside ones are used to measure the voltage signals, just as in a standard electrical resistance measurement. The main differences from a pure electrical resistance measurement are (i) the part of the specimen in-between the two voltage contacts has to be suspended, to allow temperature variation along the specimen. (ii) All the contacts should be highly thermal-conductive, to heat-sink the specimen at these points to sapphire substrate. (iii) The specimen has to be maintained in high vacuum and the whole setup be heat-shielded to the substrate temperature, to preclude heat loss through air conduction and radiation. In such a configuration, the heat generation and diffusion along the specimen can be described by the following partial differential equation and the initial and boundary conditions:

$$\rho C_p \frac{\partial}{\partial t} T(x, t) - \kappa \frac{\partial^2}{\partial x^2} T(x, t) = \frac{I_0^2 \sin^2 \omega t}{LS} [R + R' (T(x, t) - T_0)] \quad (3.4)$$

$$\begin{cases} T(0, t) = T_0 \\ T(L, t) = T_0 \\ T(x, 0) = T_0 \end{cases} \quad (3.5)$$

where C_p , κ , R and ρ are the specific heat, thermal conductivity, electric resistance and mass density of the specimen, respectively, $R' = \frac{dR}{dT}$ at substrate temperature T_0 , L , the length (between voltage contacts), and S , the cross section of the specimen.

Setting $T(x, t) - T_0$ to $T(x, t)$ will not affect the solution but simplifies the equation

and the initial and boundary conditions:

$$\frac{\partial}{\partial t}T(x, t) - a^2 \frac{\partial^2}{\partial x^2}T(x, t) - c \sin^2\omega t T(x, t) = b \sin^2\omega t \quad (3.6)$$

$$\begin{cases} T(0, t) = 0 \\ T(L, t) = 0 \\ T(x, 0) = 0 \end{cases} \quad (3.7)$$

where $a^2 = \frac{\kappa}{\rho C_p}$ is the thermal diffusivity, $b = \frac{I_0^2 R}{\rho C_p L S}$, $c = \frac{I_0^2 R'}{\rho C_p L S}$.

Using the impulse theorem, $T(x, t)$ can be represented as the integral of the specimen's responses to the instant "force", the right-side term of (3.6), at each time interval:

$$T(x, t) = \int_0^t z(x, t; \tau) d\tau \quad (3.8)$$

where $z(x, t; \tau)$ satisfies:

$$\frac{\partial z}{\partial t} - a^2 \frac{\partial^2 z}{\partial x^2} - c \sin^2\omega t z = 0 \quad (3.9)$$

$$\begin{cases} z(0, t) = 0 \\ z(L, t) = 0 \\ z(x, \tau + 0) = b \sin^2\omega \tau \end{cases} \quad (3.10)$$

Expressing $z(x, t; \tau)$ with the Fourier series of the form:

$$z(x, t; \tau) = \sum_{n=1}^{\infty} U_n(t; \tau) \sin \frac{n\pi x}{L} \quad (3.11)$$

and subtracting (3.11) into (3.9), we have

$$\sum_{n=1}^{\infty} \left[\frac{dU_n}{dt} + \left(\frac{n^2}{\gamma} - c \sin^2\omega t \right) U_n \right] \sin \frac{n\pi x}{L} = 0 \quad (3.12)$$

where $\gamma \equiv (L/\pi a)^2$.

The term $c \sin^2\omega t$ can be omitted if $n^2/\gamma \gg c$, or equivalently

$$\frac{I_0^2 R' L}{n^2 \pi^2 \kappa S} \ll 1 \quad (3.13)$$

This condition is usually well satisfied. For example, in a typical measurement $I_0=10$ mA, $R'=0.1$ Ω/K , $L=1$ mm, $S=10^{-2}$ mm², $\kappa=100$ W/m K, the left side of (3.13) is $\sim 10^{-3}$. After omitting the $c \sin^2\omega t$ term, the solution of the ordinary differential equation (3.12) is then:

$$U_n(t; \tau) = C_n(\tau) e^{-\frac{n^2}{\gamma}(t-\tau)} \quad (3.14)$$

where $C_n(\tau)$ can be determined using the initial condition in (3.10), together with the relation $\sum_{n=1}^{\infty} \frac{2[1-(-1)^n]}{n\pi} \sin \frac{n\pi x}{L} = 1$ for $0 < x < L$:

$$C_n(\tau) = \frac{2b[1-(-1)^n]}{n\pi} \sin^2 \omega \tau \quad (3.15)$$

Using (3.14) and (3.15), (3.11) becomes:

$$z(x, t; \tau) = \sum_{n=1}^{\infty} \sin \frac{n\pi x}{L} \frac{2b[1-(-1)^n]}{n\pi} \sin^2 \omega \tau e^{-\frac{n^2}{\gamma}(t-\tau)} \quad (3.16)$$

Subtract (3.11), (3.16) into (3.8) and reset $T(x, t)$ to $T(x, t) - T_0$, we have:

$$T(x, t) - T_0 = \sum_{n=1}^{\infty} \sin \frac{n\pi x}{L} \frac{\gamma b[1-(-1)^n]}{n^3 \pi} \left[1 - \frac{\cos 2\omega t + \frac{2\omega\gamma}{n^2} \sin 2\omega t}{1 + \left(\frac{2\omega\gamma}{n}\right)^2} \right] \quad (3.17)$$

where we have already dropped off the exponential term which should fastly decay out with time.

The total resistance of the specimen at temperature T_0 is:

$$R = \frac{1}{L} \int_0^L \{R + R'[T(x, t) - T_0]\} dx \quad (3.18)$$

Using (3.17) and the relation $\int_0^L \sin \frac{n\pi x}{L} dx = [1 - (-1)^n] \frac{L}{n\pi}$, resistance fluctuation with respect to R at T_0 can be expressed as:

$$R_{fl} = \sum_{n=1}^{\infty} \frac{\gamma b R' [1 - (-1)^n]^2}{n^4 \pi^2} \left[1 - \frac{\cos 2\omega t + \frac{2\omega\gamma}{n^2} \sin 2\omega t}{1 + \left(\frac{2\omega\gamma}{n}\right)^2} \right] \quad (3.19)$$

Obviously, the $n = 2$ term automatically vanishes. If only accounting the $n = 1$ term, which introduces a relative error of the order $\sim 3^{-4}$, we have:

$$R_{fl} = \frac{4}{\pi^2} \gamma b R' \left[1 - \frac{\sin(2\omega t + \phi_0)}{\sqrt{1 + (2\omega\gamma)^2}} \right] \quad (3.20)$$

where ϕ_0 satisfies:

$$\tan \phi_0 = (2\omega\gamma)^{-1} \quad (3.21)$$

The according voltage fluctuation in the presence of the *ac* current is $R_{fl} I_0 \sin \omega t$. After dropping off the *dc* term and re-define a phase constant $\phi = \frac{\pi}{2} - \phi_0$, *ac* voltage has the form:

$$V_{3\omega}(t) = \frac{2I_0^3 L R R'}{\pi^4 \kappa S \sqrt{1 + (2\omega\gamma)^2}} \sin(3\omega t - \phi) \quad (3.22)$$

$$\tan\phi = 2\omega\gamma \quad (3.23)$$

If using rms values of voltage, $V_{3\omega}$, and rms values of current, I , as what lock-in gives, (3.22) becomes:

$$V_{3\omega} = \frac{4I^3 L R R'}{\pi^4 \kappa S \sqrt{1 + (2\omega\gamma)^2}} \quad (3.24)$$

The following alternative form makes it more clearly how the 3ω signal depends on the dimensions of the specimen:

$$V_{3\omega} = \frac{4I^3 \rho_e \rho'_e}{\pi^4 \kappa \sqrt{1 + (2\omega\gamma)^2}} \left(\frac{L}{S}\right)^3 \quad (3.25)$$

where ρ_e is the electrical resistivity of the specimen, $\rho'_e = \frac{d\rho_e}{dT}$.

If accordingly only taking the $n = 1$ term in (3.17), the temperature fluctuation along the specimen is:

$$T_{fl}(x, t) = \frac{2\gamma b}{\pi} \sin \frac{n\pi x}{L} \left[1 - \frac{\sin(2\omega t + \phi_0)}{\sqrt{1 + (2\omega\gamma)^2}} \right] \quad (3.26)$$

The result is illustrated in Fig. 3.6, where $T_{fl}^0 = \pi/2\gamma b$. Obviously, temperature fluctuation reaches the maximum as $\omega\gamma \rightarrow 0$ (shown in Fig. 3.6 (a)), whereas the temperature along the specimen saturates to a time-independent distribution as $\omega\gamma \rightarrow \infty$ (Fig. 3.6 (c)).

At the high-frequency limit $\omega\gamma \gg 1$, *i.e.*, when the thermal wavelength $\lambda \ll L$, where λ is defined as $\lambda = \sqrt{\frac{a^2}{2\omega}}$, (3.24) becomes:

$$V_{3\omega} = \frac{2I^3 R R'}{\pi^2 \omega \rho C_p L S} \quad (\omega\gamma \gg 1) \quad (3.27)$$

which is the same as Holland's result [30] except for a slight difference in the numerical coefficients (*i.e.*, $\frac{2}{\pi^2}$ here *vs.* $\frac{1}{4}$ there). At this limit, however, one loses the information of thermal conductivity of the specimen. Oppositely, if taking the low-frequency limit, $\omega\gamma \ll 1$, or $\lambda \gg L$, one will only get the thermal conductivity of the specimen, but loss the information of specific heat, similar to what happened in Gahill's treatment for a two-dimensional heat diffusion problem [36]. At the low-frequency limit, $V_{3\omega}$ is frequency-independent:

$$V_{3\omega} = \frac{4I^3 R R' L}{\pi^4 \kappa S} \quad (\omega\gamma \ll 1) \quad (3.28)$$

In above derivation we have neglected the radial heat loss through radiation. Such heat loss per unit length from a cylindrical rod of diameter D can be expressed as:

$$W(x, t) = \pi \sigma D [T^4(x, t) - T_0^4] \approx 4\pi \sigma D T_0^3 [T(x, t) - T_0] \quad (3.29)$$

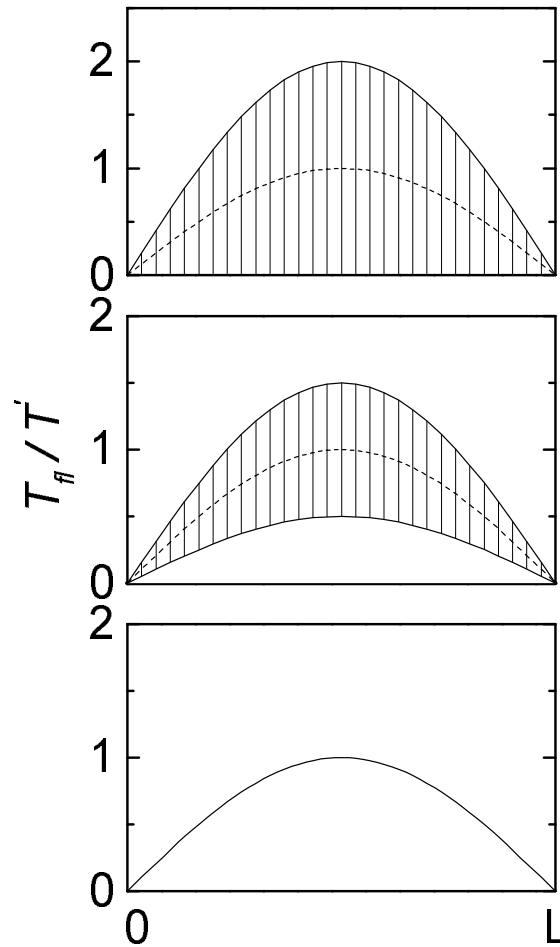


Figure 3.6: Illustration of the temperature variation along the specimen under a driving *ac* current $I_0 \sin \omega t$. The range of the variation is marked as shadowed area, which reaches the maximum at the limit $\omega\gamma \rightarrow 0$ and shrinks to a line as $\omega\gamma \rightarrow \infty$.

Equation (3.6) and (3.7) can be re-written as:

$$\frac{\partial}{\partial t}T(x, t) - a^2 \frac{\partial^2}{\partial x^2}T(x, t) (g - c \sin^2 \omega t) T(x, t) = b \sin^2 \omega t \quad (3.30)$$

$$\begin{cases} T(0, t) = 0 \\ T(L, t) = 0 \\ T(x, 0) = 0 \end{cases} \quad (3.31)$$

where $g = \frac{16\sigma T_0^3}{\rho C_p D}$. (3.12) now becomes:

$$\sum_{n=1}^{\infty} \left[\frac{dU_n}{dt} + \left(\frac{n^2}{\gamma} + g - c \sin^2 \omega t \right) U_n \right] \sin \frac{n\pi x}{L} = 0 \quad (3.32)$$

After replacing $\frac{n^2}{\gamma} + g$ with $\frac{n^2}{\gamma'}$, the final solution of (3.32) is the same as (3.22) and (3.23), except that now γ in (3.22) and (3.23) should be replaced with γ' . In the approximation of only taking the $n = 1$ term, we have: $\gamma' = \frac{\gamma}{1+g\gamma}$. Obviously, radiation heat loss can be neglected if

$$g\gamma \ll 1 \quad (3.33)$$

For cylindrical rod, (3.33) becomes: $\frac{16\sigma T_0^3 L^2}{\pi^2 \kappa D} \ll 1$. Shortening the length or increasing the diameter of the rod will help to eliminate the effect of heat loss through radiation.

Similar discussion can also be applied to account for the heat loss by remnant air. But for detailed calculation one needs to know the thermal resistance of the specimen at the surface.

3.5.2 Experimental test

The test of the above solution was carried out on two kinds of specimens: Pt wires and bundles of multiwall carbon nanotubes. The electrical resistance of the former has a positive temperature coefficient, whereas the latter a negative coefficient. Within the reasonable parameter ranges of frequency and current (we will explain it later), we do find that the $V_{3\omega}$ is proportional to $I^3 / \sqrt{1 + (2\omega\gamma)^2}$, and the phase angle $\tan\phi$ is proportional to the angular frequency. For Pt specimen, the yielded specific heat and thermal conductivity, as well as the Wiedemann-Franz ratio, do agree with the standard data over the entire temperature range measured.

We use a digital lock-in amplifier SR850 to measure the 3ω voltage signal. The block diagram of measurement is shown in Fig. 3.7. We turned off all the filters of the

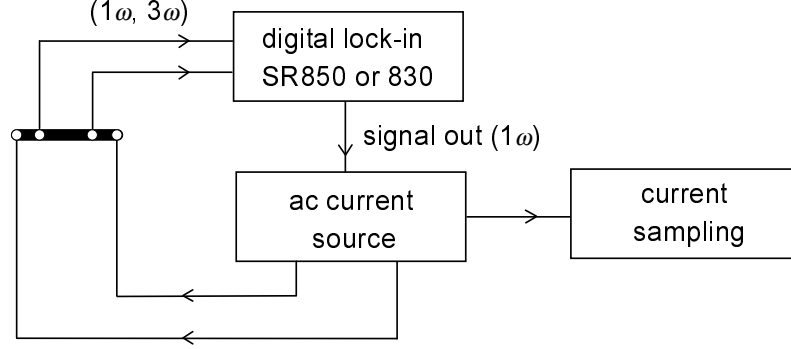


Figure 3.7: Block diagram of the measurement. We choose the digital lock-in amplifier SR850 or 830 to measure the 3ω voltage. The reference-out of the lock-in is boosted to be an *ac* current by a simple circuit (lower panel), and is then applied to the specimen. The feed-back resistor R^* should be those with very low temperature coefficient.

lock-in during the measurement, and used the *dc* coupling input mode. Before measuring the 3ω signal, the phase of the lock-in amplifier was adjusted to zero according to the 1ω signal. We use a simple electronic circuit to booster the 1ω reference-out voltage into an *ac* current feeding to the specimen. The 3ω component of the current is 10^{-4} or less comparing with the 1ω component, as checked by an HP89410A spectrum analyzer. Because the 3ω voltage signal is deeply buried in the 1ω voltage signal of many order of magnitude higher in amplitude, high dynamic reservation of the lock-in is usually required. We keep the dynamic reservation unchanged relative to the total magnification of the lock-in amplifier during the entire measurement.

There are two ways to perform the measurement. In the first way the substrate of the specimen is maintained to a few fixed temperatures. At each temperature the frequency dependence of the $V_{3\omega}$ is measured. In this way one can check whether the I^3 and the $1/\sqrt{1 + (2\omega\gamma)^2}$ dependencies of $V_{3\omega}$, as well as the $\tan\phi = 2\omega\gamma$ relation, are held.

Because $V_{3\omega} \propto I^3$, one will get much larger signal if using larger I . However, there are two reasons that prevent us from using inadequately large I . Firstly, excessive heat accumulation on the specimen will create significantly large temperature gradient at the silver paste contacts, which will violate the boundary condition in (3.5). Secondly, radiation heat loss will increase significantly as the temperature modulation is increased. In all the cases the expected relation $V_{3\omega} \propto I^3$ will no longer be held. On the other hand, the relation will also be violated if using too small I , since in the latter case $V_{3\omega}$ could be comparable to, or even smaller than, the spurious 3ω signal from the current and other

sources. In our measurement the total heating power at each measuring temperatures was maintained to be approximately equal to the value of the specimen's thermal conductivity, *i.e.*, keeping the temperature modulation to be around 1 K along the specimen.

In the second way of measurement, the temperature of the substrate is slowly ramped at a fixed rate, meanwhile the working frequency of the lock-in amplifier is switched between a few set values. The whole process, including the temperature ramping rate, the amplitude of the heating current, the frequency set-points, are all controlled by a personal computer.

For Pt specimen, we chose a wire of diameter $D = 20 \mu\text{m}$ and length $L = 8 \text{ mm}$. We found that γ of the specimen varied from 0.005 s^{-1} at 10 K to $\sim 0.2 \text{ s}^{-1}$ at room temperature, so that the working frequencies were chosen to be between 1 to 80 Hz, in order to cover the most featured frequency range of the functional form $1/\sqrt{1 + (2\omega\gamma)^2}$.

Shown in Fig. 3.8 (a) is the current dependence of the $V_{3\omega}$ at 22K, demonstrating an I^3 -law in a mediate current range. Figure 3.8 (b) and (c) show the frequency dependencies of the amplitude and the phase angle of the $V_{3\omega}$ signal at 22 K, respectively. It can be seen that the data (open circles) agree well with the predicted functional forms (solid lines). By fitting the data in Fig. 3.8 (b) to the functional form of (3.24), we get the information of thermal conductivity κ (Fig. 3.8 (d), open circles) and the time constant γ . Note that the γ thus obtained is in fairly good agreement with what the phase angle reveals *via* Eq. (3.23). Thermal diffusivity a^2 and specific heat C_p of the specimen can be obtained *via* relation $\gamma \equiv (L/\pi a)^2$ and $a^2 = \frac{\kappa}{\rho C_p}$. The results are shown in Fig. 3.8 (e) and (f) as open circles. C_p thus obtained agrees well with the standard data for Pt [39] (the solid circles in Fig. 3.8 (f)).

We notice that the measured thermal conductivity of the Pt wire only show a small peak at low temperatures, far insignificant than what is expected for high purity Pt material. Such difference is possible since κ depends largely on the purity, structural perfection, and even the dimensions of the specimen. We believed that the κ data we obtained reflect the true thermal conductivity of our Pt specimen, since the Wiedemann-Franz ratio deduced from the κ and the electrical resistivity, or more directly, from the thermal conductance and the electrical resistance, fits well to the case of pure but not totally defect-free metal samples in the whole temperature range measured [40], as shown in Fig. 3.9. The absolute value of the Wiedemann-Franz ratio is found to be $\sim 2.53 \times 10^{-8} \text{ W}\Omega/\text{K}^2$ at 290 K, slightly larger than that of the free-electron Lorenz number $2.45 \times 10^{-8} \text{ W}\Omega/\text{K}^2$, which is also in

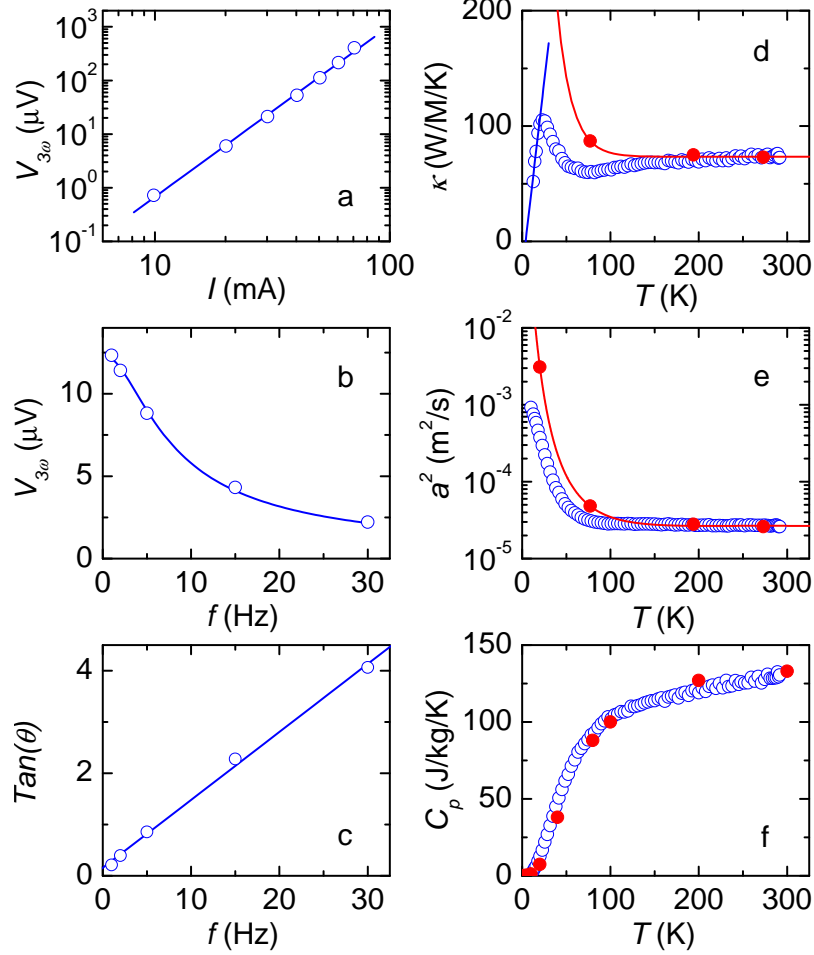


Figure 3.8: Experimental test of the 3ω method on Pt wire of 20 μm in diameter. (a) Current dependence of the $V_{3\omega}$. The open circles are the measured data, and the solid line is the predicted relation $V_{3\omega} \propto I^3$. (b) Frequency dependence of the $V_{3\omega}$ (open circles). The solid line is the predicted relation $V_{3\omega} \propto 1/\sqrt{1 + (2\omega\gamma)^2}$. (c) Frequency dependence of the phase angle of the $V_{3\omega}$ (open circles). The solid line is again the predicted relation $\tan\phi \propto \omega\gamma$. The thermal conductivity κ , thermal diffusivity a^2 , and specific heat C_p of the Pt specimen are plotted as open circles in figures (d), (e), and (f), respectively. Also shown as solid circles in these figures are the standard data of Pt [39]. The difference in κ and a^2 between our measured data and the standard data should reflect the difference in purity and/or structural perfection between the Pt specimens of different sources.

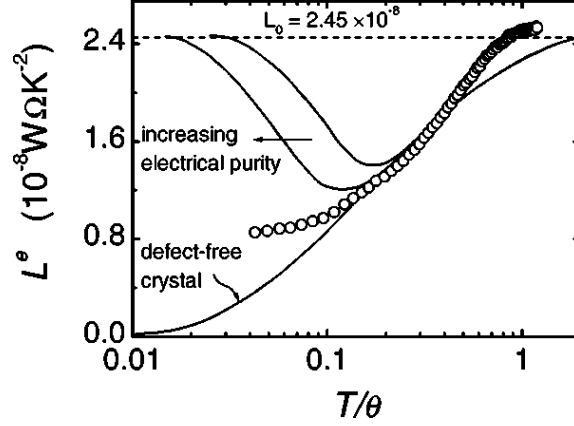


Figure 3.9: The Wiedemann-Franz ratio L^e of our Pt specimen compared with that of usual metals with different purity. The result indicates that our Pt wire specimen is pure but not totally defect-free. The room-temperature Wiedemann-Franz ratio of our Pt specimen is about $2.52 \times 10^{-8} \text{W}\Omega/\text{K}^2$, in perfect agreement with what reported in literature [40], but is slightly larger than that of the free-electron Lorenz number $L_0 = 2.45 \times 10^{-8} \text{W}\Omega/\text{K}^2$ (the dashed line). Note that for Pt its Debye temperature θ is 240 K.

perfect agreement with the previously reported value in literature [40].

Let us now examine the effect of radial heat loss through air conduction. Different sets of data in Figs. 3.10 (a), (b) and (c) were taken at different vacuum pressures. Open squares correspond to the data taking in high vacuum where slight changes (*e.g.*, a factor of 2) in vacuum pressure does not affect the results, *i.e.*, heat loss through air is absent. In poor vacuum, however, such heat loss results in spurious larger thermal conductivity and diffusivity of the specimen (open circles in Figs. 3.10 (a) and (b)). Nevertheless, it is interesting that the specific heat deduced from the κ and α^2 data is relatively insensitive to such heat loss (Figs. 3.10 (c)).

After all, let us check if the approximation conditions (3.13) and (3.33) are satisfied. We find that $\frac{I_0^2 R' L}{n^2 \pi^2 \kappa S} \sim 10^{-5}$ (taking $n = 1$). Therefore, (3.13) is well satisfied. For radiation heat loss, we find that $g \approx 0.22 \text{ s}^{-1}$ even at 300 K, and γ (actually, γ') deduced from the measurement is about 0.2 s. Therefore, $g\gamma \approx 0.044$, which means that omitting the radiation heat loss will cause about 5% of error for a 20 μm diameter Pt wire specimen with length of 8 mm.

We have also applied the 3ω method to measure the κ and C_p of multiwall carbon nanotube bundles who have a negative temperature coefficient in electrical resistivity. The bundles are about ~ 1 mm long and with a diameter ranging from $\sim 1 \mu\text{m}$ up to ~ 100

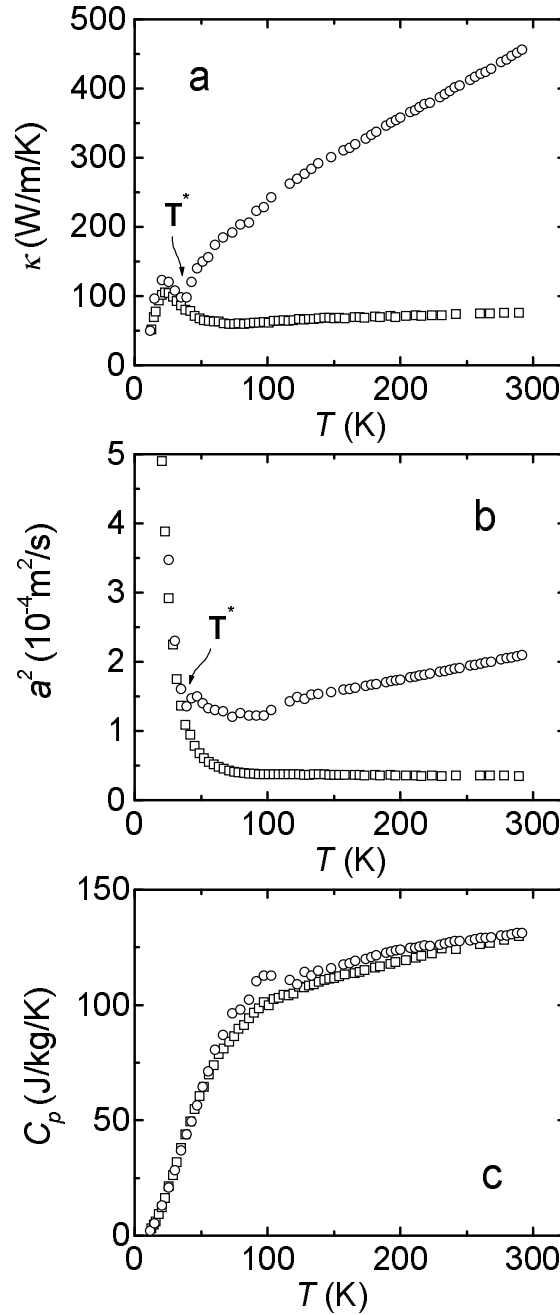


Figure 3.10: Effect of radial heat loss through air conduction. Open squares represent the case where such heat loss is absent. In one run of the measurement, radial heat loss was triggered on above T^* (marked in the figure) by distroying the vaccum of the system. The heat loss results in spurious larger thermal conductivity and diffusivity of the specimen (open circles in (a) and (b)). Nevertheless, the specific heat deduced from the κ and a^2 data is relatively insensitive to such heat loss (Fig. (c)).

μm . For these specimens, no C_p and κ data of other sources are available for comparison. Nevertheless, the frequency dependencies of $V_{3\omega}$ and $\tan\phi$ obtained on the specimens are all in good agreement with the predicted functional forms (see Fig. 3.1), which guarantees the reliability of the deduced κ and C_p . For the specimens in this measurement, $\frac{I_0^2 R' L}{\pi^2 \kappa S}$ is below 10^{-3} above ~ 60 K and is about 0.08 at 10 K, and $g\gamma$ is below 5×10^{-3} in the whole temperature range, both of which satisfy the conditions (3.13) and (3.33), respectively. For a $1 \mu\text{m}$ diametered specimen, the mass is about 10^{-9} g, which is far less than the minimum amount of mass required in any other kinds of C_p measurement.

3.5.3 Summary

We have presented an improved 3ω method after explicitly solved the heat-conduction equation under some reasonable approximations. This method can simultaneously measure the thermal conductivity and the specific heat of electrically conducting materials in a way similar to, and as simple as usual electrical resistivity measurement.

Bibliography

- [1] L. X. Benedict, S. G. Louie, and M. L. Cohen. Heat capacity of carbon nanotubes. *Solid State Commun.*, 100:177, 1996.
- [2] Z. W. Pan, S. S. Xie, B. H. Chang, C. Y. Wang, L. Lu, W. Liu, W. Y. Zhou, W. Z. Li, and L. X. Qian. Very long carbon nanotubes. *Nature*, 394:631, 1998.
- [3] Z. W. Pan, S. S. Xie, L. Lu, B. H. Chang, L. F. Sun, W. Y. Zhou, G. Wang, and D. L. Zhang. Tensile tests of ropes of very long aligned multiwall carbon nanotubes. 1999.
- [4] O. M. Corbino. Thermal oscillations in lamps of thin fibers with alternating current flowing through them and the resulting effect on the rectifier as a result of the presence of even-numbered harmonics. *Physik, Z.*, 11:413, 1910.
- [5] L. Lu, W. Yi, and Zhang Dian-lin. in preparation.
- [6] P. R. Wallace. The band theory of graphite. *Phys. Rev.*, 71:622, 1947.
- [7] J. W. Mintmire and C. T. White. Electronic and structural-properties of carbon nanotubes. *Carbon*, 33:893, 1995.
- [8] C. L. Kane and E. J. Mele. Size, shape, and low energy electronic structure of carbon nanotubes. *Phys. Rev. Lett.*, 78:1932, 1997.
- [9] W. DeSorbo and W. W. Tyler. The specific heat of graphite from 13° to 300°K. *J. Chem. Phys.*, 21:1660, 1953.
- [10] R. A. Jishi, L. Venkataraman, M. S. Dresselhaus, and G. Dresselhaus. Phonon modes in carbon nanotubules. *Chem. Phys. Lett.*, 209:77, 1993.

-
- [11] J. Yu, R. K. Kalia, and P. Vashishta. Phonons in graphitic tubules: A tight-binding molecular dynamics study. *J. Chem. Phys.*, 103:6697, 1995.
- [12] R. Saito, T. Takeya, T. Kimura, G. Dresselhaus, and M. S. Dresselhaus. Raman intensity of single-wall carbon nanotubes. *Phys. Rev. B*, 57:4145, 1998.
- [13] R. Nicklow, N. Wakabayashi, and H. G. Smith. Lattice dynamics of pyrolytic graphite. *Phys. Rev. B*, 5:4951, 1972.
- [14] K. Komatsu and T. Nagamiya. Theory of the specific heat of graphite. *J. Phys. Soc. Japan*, 6:438, 1951.
- [15] K. Komatsu. Theory of the specific heat of graphite .2. *J. Phys. Soc. Japan*, 10:346, 1955.
- [16] L. D. Landau and E. M. Lifshitz. *Course of Theoretical Physics 5, Statistical Physics*, chapter 6. Number Part 1. Pergamon Press, New York, 1980.
- [17] M. S. Dresselhaus, G. Dresselhaus, R. Saito, and A. Jorio. Raman spectroscopy of carbon nanotubes. *Phys. Rep.*, 409:47, 2005.
- [18] Y. Saito, T. Yoshikawa, S. Bandow, M. Tomita, and T. Hayashi. Interlayer spacings in carbon nanotubes. *Phys. Rev. B*, 48:1907, 1993.
- [19] X. Sun, C.-H. Kiang, M. Endo, K. Takeuchi, T. Furuta, and M. S. Dresselhaus. Stacking characteristics of graphene shells in carbon nanotubes. *Phys. Rev. B*, 54:12629, 1996.
- [20] C.-H. Kiang, M. Endo, P. M. Ajayan, G. Dresselhaus, and M. S. Dresselhaus. Size effects in carbon nanotubes. *Phys. Rev. Lett.*, 81:1869, 1998.
- [21] R. F. Service. Superstrong nanotubes show they are smart, too. *Science*, 281:940, 1998.
- [22] B. T. Kelly. *Physics of Graphite*. Applied Science Publishers, London and New Jersey, 1981.
- [23] A. M. Rao, E. Richter, S. Bandow, B. Chase, P. C. Eklund, K. A. Williams, S. Fang, K. R. Subbaswamy, M. Menon, A. Thess, R. E. Smalley, G. Dresselhaus, and M. S. Dresselhaus. Diameter-selective Raman scattering from vibrational modes in carbon nanotubes. *Science*, 275:187, 1997.

-
- [24] J. Heremans, I. Rahim, and M. S. Dresselhaus. Thermal conductivity and Raman spectra of carbon fibers. *Phys. Rev. B*, 32:6742, 1985.
- [25] S. N. Song, X. K. Wang, R. P. H. Chang, and J. B. Ketterson. Electronic properties of graphite nanotubes from galvanomagnetic effects. *Phys. Rev. Lett.*, 72:697, 1994.
- [26] L. Langer, V. Bayot, E. Grivei, J.-P. Issi, J. P. Heremans, C. H. Olk, L. Stockman, C. Van Haesendonck, and Y. Bruynseraede. Quantum transport in a multiwalled carbon nanotube. *Phys. Rev. Lett.*, 76:479, 1996.
- [27] H. Dai, E. W. Wong, and C. M. Lieber. Probing electrical transport in nanomaterials: Conductivity of individual carbon nanotubes. *Science*, 272:523, 1996.
- [28] B. Nysten, J. P. Issi, R. Barton, Jr. D. R. Boyington, and J. G. Lavin. Determination of lattice defects in carbon fibers by means of thermal-conductivity measurements. *Phys. Rev. B*, 44:2142, 1991.
- [29] For a review article see W. A. Phillips. Two-level states in glasses. *Rep. Prog. Phys.*, 50:1657, 1987.
- [30] L. R. Holland. Physical properties of Titanium. III. the specific heat. *J. Appl. Phys.*, 34:2350, 1963.
- [31] D. Gerlich, B. Abeles, and R. E. Miller. High-temperature specific heats of Ge, Si, and Ge-Si alloys. *J. Appl. Phys.*, 36:76, 1965.
- [32] L. R. Holland and R. C. Smith. Analysis of temperature fluctuations in ac heated filaments. *J. Appl. Phys.*, 37:4528, 1966.
- [33] D. G. Cahill and R. O. Pohl. Thermal conductivity of amorphous solids above the plateau. *Phys. Rev. B*, 35:4067, 1987.
- [34] N. O. Birge and S. R. Nagel. Wide-frequency specific heat spectrometer. *Rev. Sci. Instrum.*, 58:1464, 1987.
- [35] D. G. Cahill, E. Fischer, T. Klitsner, E. T. Swartz, and R. O. Pohl. Thermal conductivity of thin films: Measurements and understanding. *J. Vac. Sci. Technol. A*, 7:1259, 1989.

-
- [36] D. G. Cahill. Thermal conductivity measurement from 30 to 750 K: the 3ω method. *Rev. Sci. Instrum.*, 61:802, 1990.
 - [37] R. Frank, V. Drach, and J. Fricke. Determination of thermal conductivity and specific heat by a combined 3ω /decay technique. *Rev. Sci. Instrum.*, 64:760, 1993.
 - [38] D. H. Jung, T. W. Kwon, D. J. Bae, I. K. Moon, and Y. H. Jeong. Fully automated dynamic calorimeter. *Meas. Sci. Technol.*, 3:475, 1992.
 - [39] R. J. Corruccini and J. J. Gniewek. *CRC Handbook of Chemistry and Physics*, pages D-181. CRC Press, Boca Raton, 1988.
 - [40] J. P. Moore, D. L. McElroy, and M. Barisoni. In *Proc. 6th Thermal Conductivity Conference*, page 737, Dayton, Ohio. Air Force Materials Lab.

Chapter 4

Tunneling Spectroscopy

4.1 Motivation

Coulomb blockade (CB) has been intensively studied in a multijunction configuration, in which electron tunnel rates from the environment to a capacitively isolated "island" are blocked by the e-e interaction if the thermal fluctuation is below the charging energy $E_c = e^2/2C$ and the quantum fluctuation is suppressed with sufficiently large tunnel resistance $R_t \gg R_Q = h/2e^2$. In the case of a single-junction circuit, the understanding of CB is less straightforward. The Coulomb gap, supposed washed out for the case of low-impedance environments, should only be established if the environmental impedance exceeds R_Q .

In singlewalled carbon nanotubes (SWNTs), the reduced geometry gives rise to strong e-e interaction. Indeed, CB oscillations and evidence of Luttinger liquid (LL) have been observed [1]. In contrast to SWNTs, in which only two conductance channels are available for current transport, MWNTs with diameter in the range of 20–40 nm have several tens of conductance channels. The energy separation of the quantized subbands, given by $\Delta E = \hbar v_f/d$, is about 13–26 meV taken Fermi velocity as $v_f = 8 \times 10^5$ m/s. This value is about an order of magnitude smaller than that of SWNTs. Experiments indicate that MWNTs are considerably hole doped, thus a large number of subbands in the order of ten are occupied. The observation of weak localization [2], electron phase interference effect [3] and universal conductance fluctuations [2] support the view that low frequency conductance in MWNTs is contributed mostly by the outmost graphene shell and is characterized by 2D diffusive transport. Besides the phase interference correlated effects, strong e-e interaction has also been observed in MWNTs. There have been several

tunneling spectroscopy observations of a pronounced zero-bias suppression of tunneling density of states (TDOS) [4–6]. Moreover, the TDOS shows a power law asymptotics, i.e., $\nu(E) \sim E^\alpha$, which resembles the case of a LL. It is noteworthy that in the Environmental Quantum Fluctuation (EQF) theory, for a single tunnel junction coupled to high-impedance transmission lines, such a scaling behavior is also predicted in the limit of many parallel transmission modes [7]. The physical origin of these power laws is the linear dispersion of bosonic excitations that are characteristic both for LL, which is strictly 1D ballistic conductor, and a single tunnel junction connected to a 3D disordered conductor. In the latter case the quasi particle tunneling is suppressed at $V \ll e/2C$, therefore the charge is transported with 1D plasmon modes. The facts that MWNTs have many conductance modes, as well as the observation of a crossover from power law to Ohmic behavior at higher voltages [5], suggests that EQF theory is more appropriate to describe the observed TDOS renormalization. Most of these measurements were done in multi-junction configurations. Therefore a single tunnel junction measurement is needed to further clarify this issue.

4.2 Experimental

In this chapter, millimeter-long CVD-grown MWNTs [8] are measured by a cross-junction method. The MWNTs samples are composed of loosely entangled nanotubes that are roughly parallel to each other and extend up to 2 mm long. The single tunnel junctions are formed by crossing a very thin ($< 1 \mu\text{m}$) MWNTs bundle on a narrow strip of metal wire fabricated on an insulating substrate. We explored different electrode materials including Au, Cu, Sn, and Al. In the case of Sn and Al, a small magnetic field was applied to suppress the Superconducting state below T_c . No obvious change of device characteristics caused by the choice of metals was observed. With such a cross-junction configuration the measured conductance is only contributed by the tunnel junction itself, since the current is passed along one arm of the MWNT/metal and voltage is measured along the other non-current carrying arm. Thus the device can be understood as a small number of single junctions in parallel. Despite the simplicity of the fabrication method, we found that the devices made are very stable and sustain several cooling cycles without apparent change of characteristics. More than 20 samples we measured all yield strong zero bias suppression of TDOS.

The current $I(V)$ as well as $G \equiv dI/dV$, are calculated by a golden-rule approach incorporating the environmental influence by $P(E)$, the probability for a tunneling electron

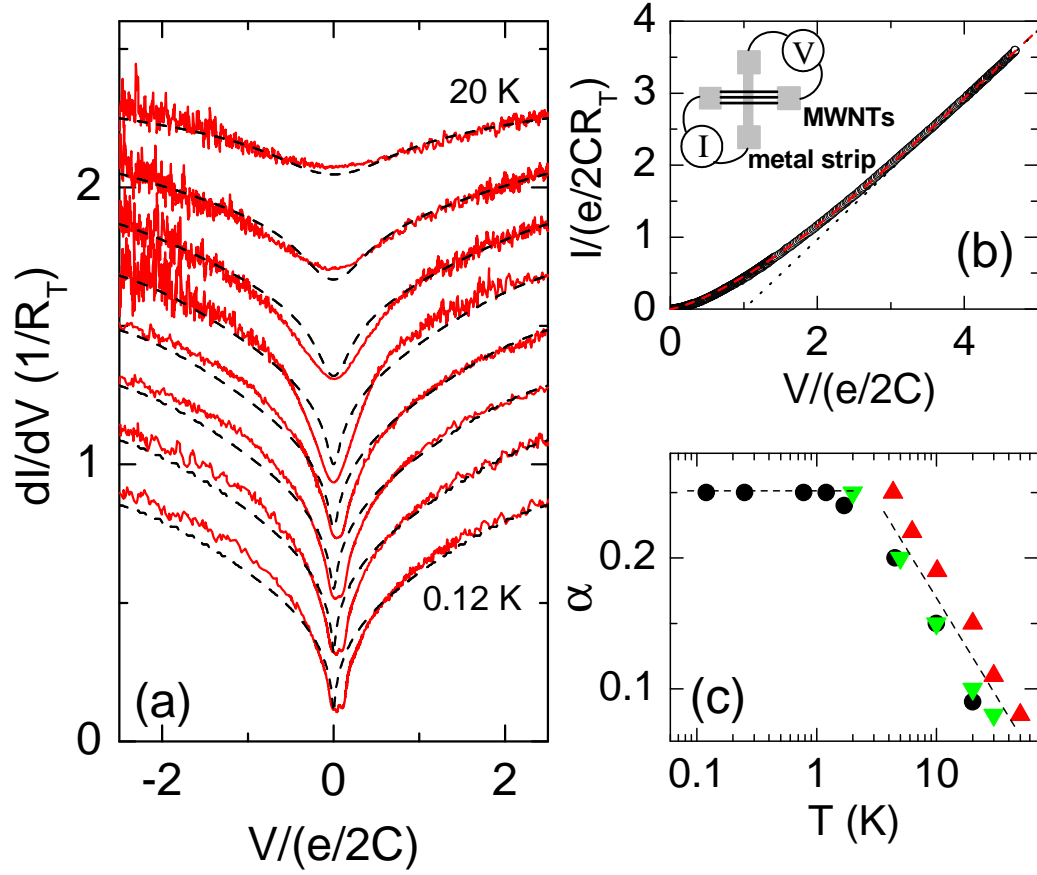


Figure 4.1: (a) dI/dV as a function of V in dimensionless units measured at $T = 0.12, 0.25, 0.78, 1.2, 1.7, 4.5, 10, 20$ K (sample 990530s6). Dashed lines are the fits of EQF theory. (b) DC current simultaneously measured at 0.12 K. Dashed line is the numerical fit. Dotted line shows a Coulomb offset of $e/2C$. (c) Temperature dependence of the exponent α for three samples (\circ : 990530s6; \triangle : 990316; ∇ : 990320).

to lose energy to the environment. $P(E)$ can be calculated from its Fourier transform, the phase correlation function $J(t)$. In the transmission-line model, $J(t)$ is determined by the total environmental impedance

$$Z_t(\omega) = (i\omega C + Z^{-1}(\omega))^{-1} \quad (4.1)$$

where $Z(\omega)$ is the external environmental impedance. We applied the method in Ref. [9] to evaluate $P(E)$ from an integral equation without the need of going to the time domain. The I-V characteristics are then calculated for finite temperatures and arbitrary junction impedance. The parameters that appear in the numerical calculation are the damping strength

$$\alpha = Z(0)/R_Q, \quad (4.2)$$

the inverse relaxation time ω_{RC} , and the quality factor

$$Q = \omega_{RC}/\omega_S \quad (4.3)$$

with the resonance frequency of the undamped circuit $\omega_S = (LC)^{-1/2}$. It is noted that the quality factor Q only plays a minor role as an additional adjustable parameter. Therefore it is not important to the fit, and is set always to unit.

4.3 Discussion

We then tried to fit our experimental data with the EQF theory. Since E_c and R_t are determined by the high-voltage data, the isolation resistance $R_{iso} = Z(0)$ is the only adjustable parameter in our fitting. In contrast to the case of Ref. [10], where R_{iso} is formed by ideal Ohmic and temperature-independent resistors, R_{iso} in our case are provided by the resistive impedance of the MWNTs themselves, which should be temperature-dependent. From the fitting, we do see an evolution of α from 0.1 at 20 K to 0.25 at 1–4 K and then α saturates (Fig. 4.1c). Note that dimensionless units are used with G normalized by $1/R_t$ and voltage normalized by $e/2C$. Therefore the number of the single tunnel junctions has no effect on the fitting and results on different samples can be directly compared. We found that for different samples with scattered characteristics (see Table 4.1), at low temperatures the exponent α reaches an universal value of 0.25–0.35, which agrees with previous multi-junction measurements [5, 6]. It yields $R_{iso} = 3.3\text{--}4.6\text{ k}\Omega$ that is roughly a constant for

Table 4.1: A partial list of characteristics of the samples.

Sample	R_t (k Ω)	E_c (eV)	C (aF)	R_{iso} (k Ω)	α
990316	18.4	0.019	4.2	3.3 ^a	0.25 ^a
990320	48.3	0.014	5.7	3.3 ^a	0.25 ^a
990530s6	8.6	0.01	8.0	3.3 ^a	0.25 ^a
990530s1	10.0	0.02	4.0	4.6 ^a	0.35 ^a
990202	9.1	0.004	20.0	3.5 ^a	0.27 ^a

^a Value acquired at $T = 1.2\text{--}4.3$ K.

different samples. This coincidence is not accidental but reflects the intrinsic electrodynamic modes of the MWNTs, which can be modeled as an ideal resistive LC transmission line:

$$R = (L'/C')^{1/2} \quad (4.4)$$

with the kinetic inductance $L' = R_Q/2Nv_f$ estimated as ≈ 1 nH/ μm for $N \approx 10\text{--}20$ modes and the capacitance $C' \approx 20\text{--}30$ aF/ μm . Therefore, the “environment” with respect to the single-junctions in our devices is provided by MWNTs themselves, not the external circuits.

As mentioned previously, for an isolated single tunnel junction with many parallel transport modes, the EQF theory predicts a power-law asymptotics:

$$G(V, T)/G(0, T) \equiv f(V/T) = |\Gamma[\frac{\alpha}{2} + \frac{ieV}{2\pi k_B T}]/\Gamma[\frac{\alpha}{2}]\Gamma[1 + \frac{ieV}{2\pi k_B T}]|^2 \quad (4.5)$$

where $G(0, T)$ is the zero-bias conductance [10]. For $eV/2\pi k_B T \gg 1$, a voltage power law $G(V, T) \sim V^\alpha$ is expected. Note that in the above scaling function, exponent α is the only adjustable parameter. In a two-junction configuration, an additional parameter was introduced to take into account the voltage division between the two tunnel junctions [1]. Seen in Fig. 4.2, we do observe such a scaling behavior. Here $f(V/T)$ represented by solid line is calculated taken $\alpha = 0.27$. The inset shows the original data in which the dashed line is calculated numerically using the same exponent $\alpha = 0.27$.

CB and Coulomb gap effects in MWNTs are recently described with microscopic theories in Refs. [14,15]. In the 2D diffusive regime, the exponent for tunneling into the bulk of a MWNT is

$$\alpha = (R/h\nu_0 D) \ln(1 + \nu_0 U_0) \quad (4.6)$$

Here R is the tube radius, U_0 is the intratube Coulomb interaction, $D = v_f^2 \tau/2$ is the charge diffusivity, and the “bare” DOS $\nu_0 = N/4h v_f$ with $N \approx 20$. If we use $v_f \tau \approx 60$ nm from the

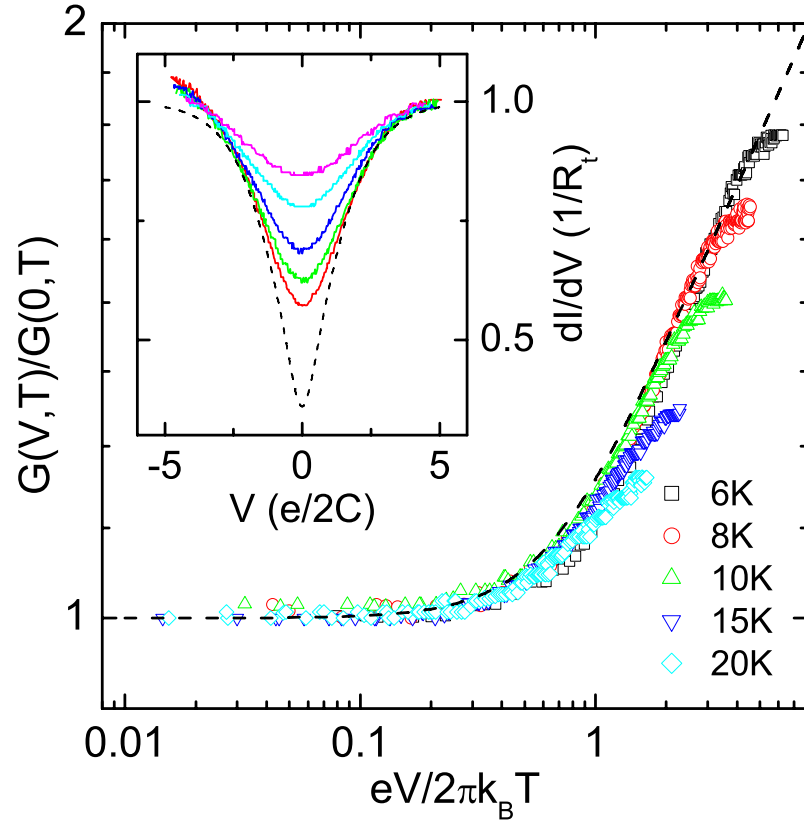


Figure 4.2: Scaled conductance $G(V,T)/G(0,T)$ of another sample (990202). The inset shows the original dI/dV vs V with the dashed line calculated with exponent $\alpha = 0.27$.

magnetoresistance data [11] and taking $R \approx 20$ nm, then under the condition of $U_0/hv_f \sim 1$ the above formula yields $\alpha \approx 0.25$, which agrees with our experiment.

4.4 Fano resonance

Besides the voltage power-law phenomenon, which is characteristic of strong Coulomb interactions, another energy scale “the discrete energy levels due to electron confinement” emerges as temperature decreases, and it modifies the tunneling spectra. Unlike the case of a two-junction configuration, where the electrons are confined by the two contacts if the nanotube is clean enough, in a single-junction configuration the electrons can be confined by disorders when the MWNTs are “dirty”, such that the impedance of the local environment of the junction is larger than R_Q . A stacking mismatch between adjacent walls and other structural imperfections are possible sources of disorders in MWNTs, resulting in discrete energy levels.

By cooling down the devices to even lower temperatures, we observe that G develops a narrow resonance-like anomaly at very low bias (Fig. 4.3). The asymmetric anomaly builds up consistently with the decrease of temperature and even shows a dip structure. The line shape resembles that of a Fano resonance, which is ubiquitous in resonant spin-flip scattering. Fano resonance happens when there are two interfering scattering channels: a discrete energy level and a continuum band. It has recently been rediscovered in mesoscopic systems such as semiconductor quantum dots, SWNTs, etc. [12–14]. Taking a quantum dot as an example, it can be considered as a gate-confined droplet of electrons with localized states. The coupling of the dot to the leads can be tuned in a controllable way to enter different transport regimes: If the dot is weakly coupled from the environment, a well-established CB is developed. The charge transport is suppressed except for narrow resonances at charge degeneracy points. When the tunnel barriers become more transparent, the dot enters Kondo regime, i.e., below a characteristic Kondo temperature T_K , spin-flip co-tunneling events introduce a narrow symmetric TDOS peak at E_F that can be interpreted as a discrete level. If the coupling is strong enough, the interference between this discrete level and the conduction continuum give rise to an asymmetric Fano resonance. In Ref. [12], such a crossover from a well-established CB through Kondo regime to Fano regime has been clearly observed.

We found that the asymmetric resonance line shape of G can be fitted by the

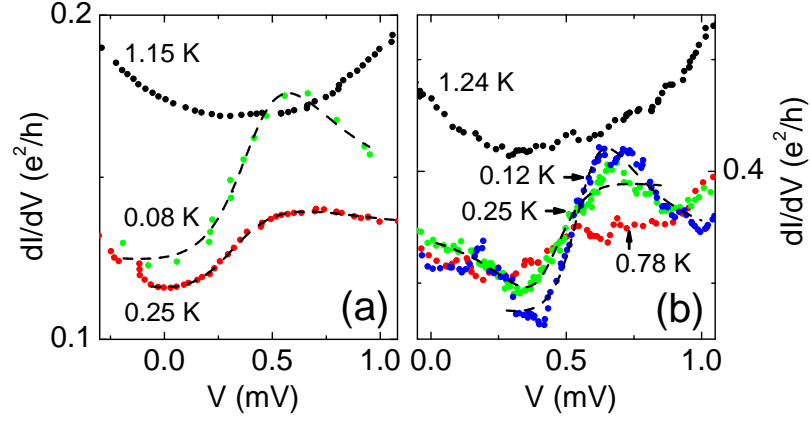


Figure 4.3: Asymmetric resonance features of dI/dV seen in two samples: 990530s1(a) and 990530s6(b). Dashed lines are the fits of Fano's formula.

Table 4.2: Characteristics of the two samples in Fig. 4.3

Sample	T (K)	q	ε_0 (meV)	Γ (meV)	T_K (K)
990530s6	0.25	0.53	0.43	0.32	1.86
990530s6	0.12	1.75	0.57	0.29	1.68
990530s1	0.25	0.92	0.3	0.65	3.77
990530s1	0.08	1.97	0.43	0.56	3.25

Fano's formula:

$$G \propto (E + q)^2 / (E^2 + 1) \quad (4.7)$$

Here q is the so-called asymmetry parameter. $E = (\varepsilon - \varepsilon_0)/(\Gamma/2)$ is the dimensionless detuning from resonance. As expected, the asymmetry parameter q as a measure of the degree of coupling between the discrete state and the continuum increases when the temperature drops. The Kondo temperature, estimated from the relation $\Gamma = 2k_B T_K$, is consistent for a device at different temperatures, and agrees with the observed FWHM of the resonance.

If Kondo physics really accounts, then G at voltage near resonance should show a non-monotonic temperature dependence around T_K [14]. A close look at I-V curves (Fig. 4.3) does exhibit such a behavior: G at the peak position first drops with T and then rise up below ~ 1 K. The conductance measured at zero bias, however, shows a monotonic temperature dependence (Fig. 4.4b), which is expected when measuring at energies out of the Fano resonance. Moreover, we found that a perpendicular magnetic field B shows two-folded effects (Fig. 4.4a and 4.4c): Firstly the background conductance monotonically increases with the applied B . Secondly, the dip seen at zero field gradually disappears and

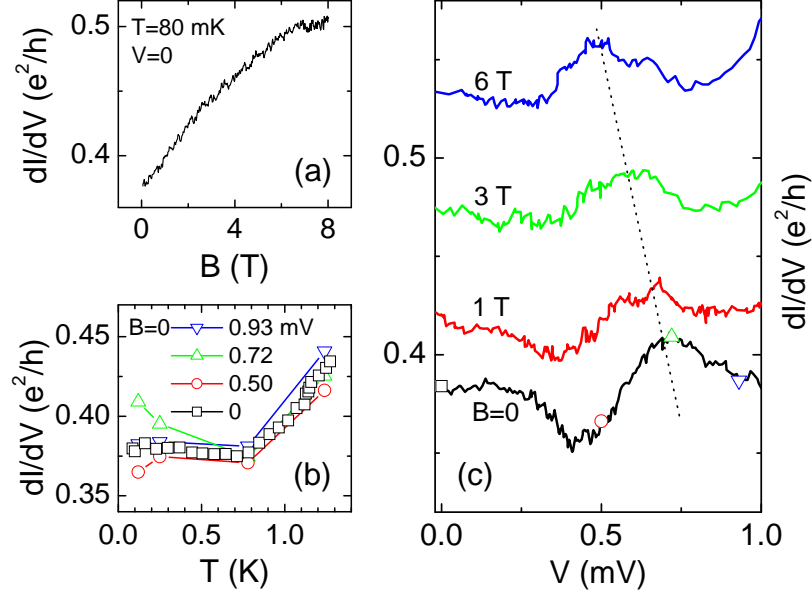


Figure 4.4: (a) The dependence of zero-bias dI/dV on perpendicular magnetic field. (b) The temperature dependence of dI/dV measured at different voltages. (c) Effect of perpendicular magnetic field. From bottom to top: $B = 0, 1, 4, 8$ Tesla (sample 990530s6).

the resonance turns into a nearly symmetric peak at high field, similar to what was observed in the semiconductor quantum dots [12]. The magnetic field effect can be explained with the following pictures: Firstly adding a flux should change the amplitude and/or the phase for the resonant channels therefore breakdown the coherent backscattering and increase the forward transmission through the channel. Secondly, the magnetic field can destroy the interference between the resonant and nonresonant path, transforming a resonant dip into a peak.

Since Kondo physics is historically interpreted as the interplay between the d -orbitals of magnetic impurities and the conduction continuum, we have to exclude the possibility that the observed Fano resonance come from the residual Fe/Si catalyst in the MWNTs samples. It has been shown that magnetic impurities in MWNTs cause an enhancement of thermoelectric power [15], which is absent in our careful TEP measurement [16]. Furthermore, no Fe signature in the body of MWNT bundles could be detected within the instrumental resolution in the X-ray and TEM studies. Therefore the observed Fano resonance should be inherent property of MWNTs, which can be virtually treated as quantum dots strongly coupled to the leads. We noticed that recently Buitelaar et al. have also

seen clear traces of CB and Kondo resonance in MWNT SET devices [17]. Their observed Kondo temperature $T_K = 1.2$ K is in good agreement of our results.

4.5 Summary

In summary, strong zero-bias suppression of TDOS is observed in MWNTs single tunnel junctions that can be well explained with the EQF theory. The observed exponent $\alpha \approx 0.25\text{--}0.35$ is found to be consistent for all the samples. Reinforced by the observation of Altshuler-Aronov-Spivak (AAS) oscillations in magnetoresistance measurements (presented in the next chapter), we interpret MWNTs as a quasi-2D diffusive molecular quantum wire in which both disorder and intrinsic Coulomb interaction play important role in low-energy excitations. Similar to the case of an open quantum dot, in low-impedance junctions we found that a Fano-resonance like asymmetric conductance anomaly is built up below meV energy scales. The coexistence of abundant mesoscopic phenomena exhibits that MWNTs provide a good laboratory for the study of electron interactions in mesoscopic system.

Bibliography

- [1] M. Bockrath, D. H. Cobden, J. Lu, A. G. Rinzler, R. E. Smalley, L. Balents, and P. L. McEuen. Luttinger-liquid behaviour in carbon nanotubes. *Nature*, 397:598, 1999.
- [2] L. Langer, V. Bayot, E. Grivei, J.-P. Issi, J. P. Heremans, C. H. Olk, L. Stockman, C. Van Haesendonck, and Y. Bruynseraede. Quantum transport in a multiwalled carbon nanotube. *Phys. Rev. Lett.*, 76:479, 1996.
- [3] A. Bachtold, C. Strunk, J.-P. Salvetat, J.-M. Bonard, L. Forró, T. Nussbaumer, and C. Schönenberger. Aharonov-Bohm oscillations in carbon nanotubes. *Nature*, 397:673, 1999.
- [4] J. Haruyama, I. Takesue, and Y. Sato. Coulomb blockade in a single tunnel junction directly connected to a multiwalled carbon nanotube. *Appl. Phys. Lett.*, 77:2891, 2000.
- [5] R. Tarkiainen, M. Ahlskog, J. Penttilä, L. Roschier, P. Hakonen, M. Paalanen, and E. Sonin. Multiwalled carbon nanotube: Luttinger versus Fermi liquid. *Phys. Rev. B*, 64:195412, 2001.
- [6] A. Bachtold, M. de Jonge, K. Grove-Rasmussen, P. L. McEuen, M. Buitelaar, and C. Schönenberger. Suppression of tunneling into multiwall carbon nanotubes. *Phys. Rev. Lett.*, 87:166801, 2001.
- [7] G.-L. Ingold and Y. V. Nazarov. *Single Charge Tunneling*, chapter 2, pages 21–107. NATO ASI Series. Plenum Press, New York, 1991.
- [8] Z. W. Pan, S. S. Xie, B. H. Chang, C. Y. Wang, L. Lu, W. Liu, W. Y. Zhou, W. Z. Li, and L. X. Qian. Very long carbon nanotubes. *Nature*, 394:631, 1998.

-
- [9] G.-L. Ingold and H. Grabert. Finite-temperature current-voltage characteristics of ultrasmall tunnel-junctions. *Europhys. Lett.*, 14:371, 1991.
 - [10] W. Zheng, J. R. Friedman, D. V. Averin, S. Han, and J. E. Lukens. Observation of strong Coulomb blockade in resistively isolated tunnel junctions. *Solid State Comm.*, 108:839, 1998.
 - [11] W. Yi et al. unpublished data.
 - [12] J. Göres, D. Goldhaber-Gordon, S. Heemeyer, M. A. Kastner, H. Shtrikman, D. Mahalu, and U. Meirav. Fano resonances in electronic transport through a single-electron transistor. *Phys. Rev. B*, 62:2188, 2000.
 - [13] W. G. van der Wiel, S. De Franceschi, T. Fujisawa, J. M. Elzerman, S. Tarucha, and L. P. Kouwenhoven. The Kondo effect in the unitary limit. *Science*, 289:2105, 2000.
 - [14] J. Nygård, D. H. Cobden, and P. E. Lindelof. Kondo physics in carbon nanotubes. *Nature*, 408:342, 2000.
 - [15] L. Grigorian, G. U. Sumanasekera, A. L. Loper, S. L. Fang, J. L. Allen, and P. C. Eklund. Giant thermopower in carbon nanotubes: A one-dimensional Kondo system. *Phys. Rev. B*, 60:R11309, 1999.
 - [16] N. Kang, L. Lu, W. J. Kong, J. S. Hu, W. Yi, Y. P. Wang, D. L. Zhang, Z. W. Pan, and S.S. Xie. cond-mat/0202065.
 - [17] M. R. Buitelaar, A. Bachtold, T. Nussbaumer, M. Iqbal, and C. Schönenberger. Multiwall carbon nanotubes as quantum dots. *Phys. Rev. Lett.*, 88:156801, 2002.

Chapter 5

Transport Properties

5.1 Thermoelectric power

5.1.1 Introduction

The thermoelectric power is an important transport property of solids. The basic picture of thermoelectric effect (or Seebeck effect) in a conductive solid is the carrier diffusion in the presence of a temperature gradient. The specimen is considered as a vessel filled with a gas of free electrons and/or holes, and when a temperature gradient $\Delta_x T = dT/dx$ is applied, conduction electrons and/or holes are thermally drifted in the $-x$ direction, so as to setup an electric field E_x as well as a thermoelectromotive force (TEF)

$$V_x = \int_0^x E_x dx \quad (5.1)$$

The thermoelectric power (TEP) or Seebeck coefficient is defined by

$$S = \frac{E_x}{\Delta_x T} = \frac{dV_x}{dT} \quad (5.2)$$

In the case of a two-carrier system, electrons and holes give rise to polarizations opposite to each other, so that $S < 0$ when electrons predominate over holes in the contribution, and vice versa.

In the above discussion, the internal structure characters of materials are not taken into account. In actual solids, thermal vibrations of atoms can be described as combined elastic lattice wave, or in the quantum mechanical expression, these lattice waves are considered as phonons. In absense of electron-phonon interactions, a specimen can be looked

on as a vessel of electron and phonon gases in which two constituents diffuse separately in the presence of a temperature gradient. However, in actual solids the momentum of the drifting carriers is irreversibly transferred to phonons and give rise to electrical resistance and Joule heating. In the thermoelectric effect, since the drift takes place in the same direction for both systems, phonons may transfer their momentum to carriers so as to enhance the polarization. Such a mechanism, the so-called phonon drag effect, has been manifested in a variety of solid materials.

Since carbon nanotube can be considered as wrapped-up graphite sheets, it is helpful to discuss the thermoelectric power of graphite firstly. The well crystallized graphite is a nearly compensated material, therefore the diffusive component of TEP is very low and its sign changes very sensitively, reflecting the delicate balance between electrons and holes. When the electronic structure is concerned, graphite is a semimetal in which the phonon drag effect is pronounced due to the following reasons. Firstly, the electron-phonon coupling which participates directly in the drag effect is very strong. Secondly, the wave vectors of the phonons, which play a dominant role in the drag effect, are small due to the small Fermi surface of graphite. Therefore the phonon-phonon collisions establishing equilibrium phonon distribution is not strong enough to diminish the phonon drag effect. As a result, the basal-plane TEP of graphite has a pronounced phonon drag induced dip at about 30K, at which the average wavenumber of the in-plane mode phonons is found to equal the Fermi wavenumber.

5.1.2 Experimental

We use a standard comparative method to measure the TEP and thermal conductivity of a MWNT bundle sample simultaneously. The measurement configuration is shown in Fig. 5.1. The sample was placed in series with a standard constantan (TN) rod between the electric heater and the heat sink. Two chromel (KP) wires were attached to the constantan rod to form a thermocouple. Assuming that there were no heat losses, i.e., the same heat flow passes through the constantan rod and the sample. Four Au electrical leads were attached to the sample with silver paint so that successive measurement of electrical resistance could be performed on the same sample. Chromel-constantan thermocouple leads were attached with high thermal-conductive epoxy at the same place with the voltage leads. TEP and thermal conductance was measured at fixed temperatures by heating the far end

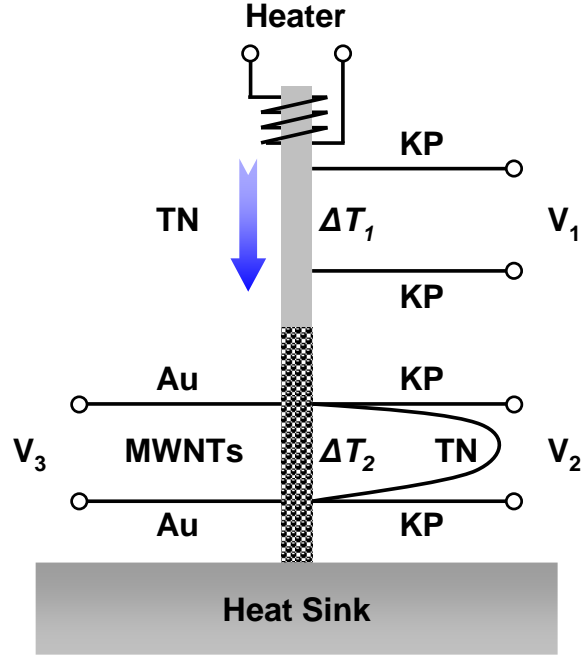


Figure 5.1: Schematic of experimental configuration for TEP measurement. The two Au current leads for four-probe resistance measurement are not shown.

of the constantan rod with triangle-wave formed currents at very low frequencies (i.e., 0.01 Hz). By comparing different voltages induced on the constantan rod and the sample, we obtained the thermal conductance of the tubes.

According to the formula of Seebeck effect, S of two chromel-constantan thermocouples and MWNT sample are as follows

$$V_1 = (S_{TN} - S_{KP})\Delta T_1 \quad (5.3)$$

$$V_2 = (S_{TN} - S_{KP})\Delta T_2 \quad (5.4)$$

$$V_3 = (S_{MWNT} - S_{Au})\Delta T_2 \quad (5.5)$$

The heat currents flow in the constantan rod and MWNT bundle could be written as

$$Q_1 = -\kappa_{TN}A_1\Delta T_1/L_1 \quad (5.6)$$

$$Q_2 = -\kappa_{MWNT}A_2\Delta T_2/L_2 \quad (5.7)$$

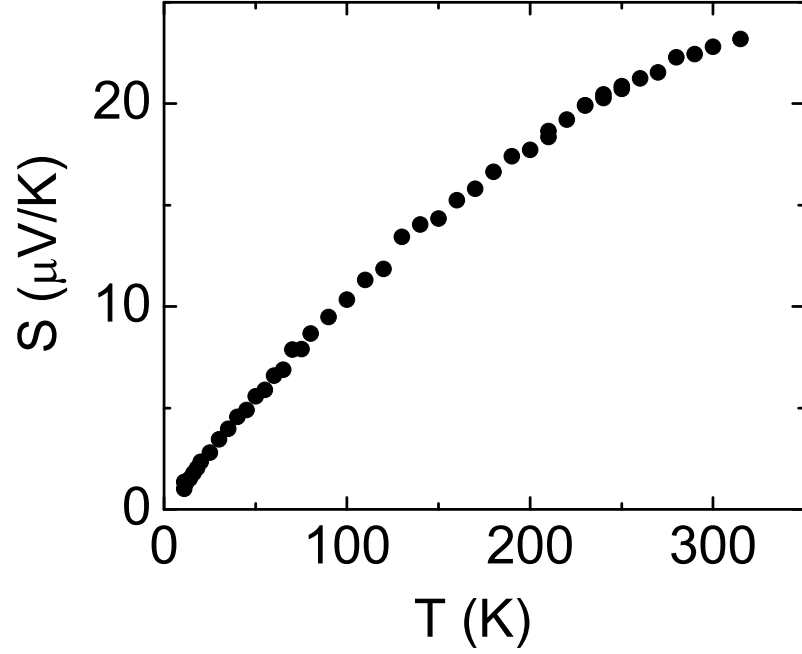


Figure 5.2: TEP of a MWNTs sample measured from 10 K to 300 K.

Here A_1 and A_2 are cross-sectional area of the constantan rod and MWNT bundle separately. L_1 and L_2 are their length. Assuming that there were no heat losses at the interface between the constantan rod and the MWNT sample, i.e., $Q_1 = Q_2$, S and κ of MWNT sample can be derived

$$S_{MWNT} = S_{Au} + (S_{TN} - S_{KP})V_3/V_2 \quad (5.8)$$

$$\kappa_{MWNT} = \kappa_{TN}(A_1L_2/A_2L_1)V_1/V_2 \quad (5.9)$$

Shown in Fig. 5.2 are the results of our measurement. TEP of MWNTs is moderately large, approaching $\sim 20 \mu\text{V/K}$ at room temperature. The sign of TEP is positive, indicating that holes predominate over electrons in the contribution. At low temperatures, TEP has a nearly linear temperature dependence and approaches zero as $T \rightarrow 0$, which is a character of metallic behaviors. At high temperatures TEP tends to be saturated. Such a large positive thermoelectric power of MWNTs gives strong evidence that the electron-hole symmetry in metallic nanotubes is broken. Similar results on SWNT ropes were reported by Hone et al. [1]. At the present stage, the origin of such symmetry breaking is unclear. Hone et al. suggested that the electron-hole symmetry is broken due to inter-tube hopping

when the tubes are assembled into ropes. However, our MWNTs are well decoupled from each other, therefore such a mechanism is not appropriate. Other mechanisms, such as carrier interactions with disorder and defects, might play important roles in TEP.

The data of thermal conductivity (not presented) is qualitatively similar to that derived by 3ω method. In most of the temperature range measured, κ is nearly linear. The order of magnitude of κ is the same with that derived by 3ω method, giving a convincing proof that 3ω method is very reliable.

5.2 Magnetoresistance

In this section, the dependence of the electrical resistance of MWNTs on longitudinal magnetic field (parallel to tube axes) has been studied. Without access of lithographic micro-fabrication facilities, we prepared the devices by the following method: A thin bundle of MWNTs was laid on a sapphire substrate with parallel chromium electrodes separated with each other by $4\text{ }\mu\text{m}$. Then a zircite wafer with a layer of single-sided Scotch tape was pressed on the sample by a tiny screw. The Scotch tape was used to prevent the breaking of the sample. By adjusting the magnitude of pressure, good electrical contacts could often be made. The room-temperature two-probe resistance of the samples range from several tens $\text{k}\Omega$ to $1\text{ M}\Omega$. The experiment was conducted in a dilution refrigerator with a superconducting magnet (Oxford Instruments 200 TLM). Figure 5.3 shows a typical longitudinal magnetoresistance (MR) measurement. When a magnetic field B is applied, the resistance of MWNTs decreases. This negative MR is associated with the phenomenon of weak localization (WL). WL originates from the enhancement of backscattering which contains interference terms adding up constructively in zero field. In a specific geometry like a diffusive and thin-walled metallic cylinder (or ring), the WL contribution is periodic in the magnetic flux through the cylinder with period $h/2e$, known as Altshuler-Aronov-Spivak (AAS) effect [2,3]. In Fig. 5.3, it can be clearly seen that the resistance has a second maximum at $B = 3\text{ T}$ and a third maximum at $B = 6\text{ T}$. From TEM images, the average outermost diameter of our MWNTs is 30 nm , the corresponding period of AAS oscillations is 2.93 T , which is in good agreement with the observation.

Besides the reproducible resistance oscillations, non-reproducible temporal resistance jumps are often observed (Fig. 5.4). We note that Bachtold et al. observed similar jumps in measurements on individual MWNTs. They suggested that temporal changes in

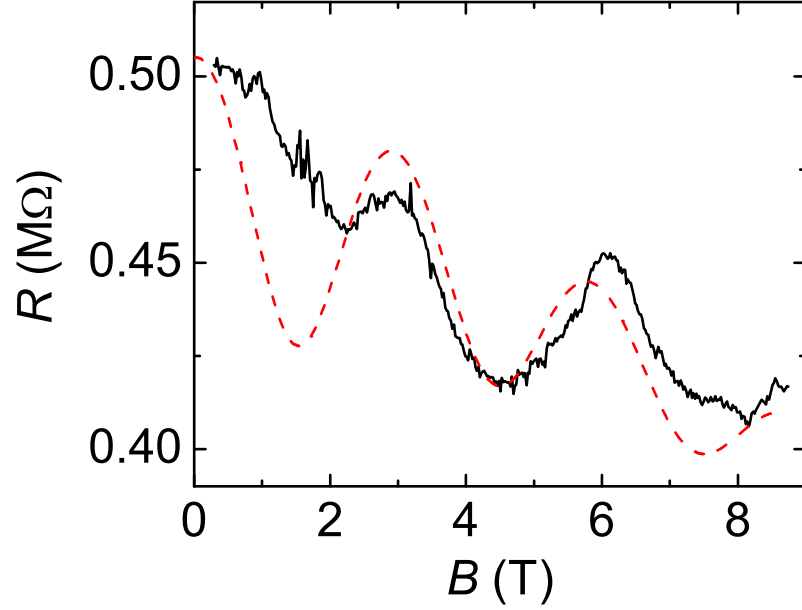


Figure 5.3: Longitudinal Magnetoresistance of a MWNTs sample at 20 mK (solid curve). The temporal resistance jumps of the bare data have been removed. The dashed curve corresponds to theoretical prediction for the quantum correction to the resistance of a thin-walled cylindrical conductor using the parameters mentioned in the text.

the electric contacts, defects or impurities in the nanotubes are possibly responsible for these jumps. However, we note that the magnitudes of these temporal resistance jumps are integer multiples of $h/2e^2$. Therefore, the resistance jumps probably correspond to the opening or closing of the conducting channels of a MWNT. Further investigations are needed to clarify this problem.

Now let's compare our experimental data with the theory of AAS effect [2, 4]. Firstly we consider a single graphene cylinder with radius R and longitudinal height b , which approximately equals to the distance between the electrical contacts. Then two parameters appear in the AAS theory: the temperature-dependent phase-coherence length L_φ and the mean free path l . Following the formula given by Altshuler, Aronov, and Spivak, the correction of longitudinal DC conductance is

$$\Delta G = -\frac{e^2}{\pi^2 \hbar} \frac{2\pi R}{b} \left[\ln \frac{L_\varphi}{l} + 2 \sum_{n=1}^{\infty} K_0\left(n \frac{2\pi R}{L_\varphi}\right) \cos\left(2\pi n \frac{2\phi}{\phi_0}\right) \right] \quad (5.10)$$

where $K_0(x)$ is the modified Bessel function. The conductance correction oscillates with a period $\phi_0/2$, becoming exponentially small for $L_\varphi \ll 2\pi R$.

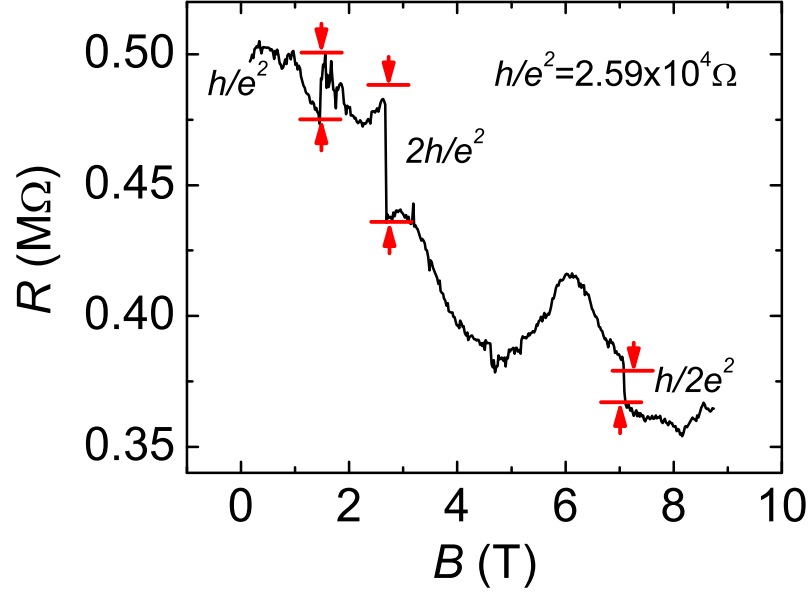


Figure 5.4: The raw data of the same sample as in Fig. 5.3. Temporal resistance jumps with magnitude $h/2e^2$, h/e^2 and $2h/e^2$ can be clearly seen.

In Eq. 5.10 the wall thickness was not taken into account. In the real samples the field in the cylinder walls is not negligible. As a result, the oscillations decay as the field increases and a monotonic component appears in the magnetic field dependence of the sample resistivity. Moreover, the magnetic field direction may deviate from the axis of cylinder by a small angle θ , making the effective wall thickness a^* larger than the actual value a . The inclusion of magnetic field results in the phase relaxation length L_φ becoming field dependent. For a cylinder with an effective wall thickness a^* in a parallel field,

$$\frac{1}{L_\varphi^2} = \frac{1}{D\tau_\varphi} + \frac{1}{3} \left(\frac{a^* e H}{\hbar} \right)^2 \quad (5.11)$$

where a^* is given by

$$a^{*2} = a^2 \cos^2 \theta + 6R^2 \sin^2 \theta \quad (5.12)$$

Matching the theory to the measurement at $T = 20$ mK, we obtain $L_\varphi \approx 63$ nm, $l \approx 1$ nm, $\theta = 4.4^\circ$. The agreement between theory (dotted line) and experiment (solid line) is quite good except for the low field part. This agreement is obtained when assuming that only one graphene cylinder contributes to the conductance, i.e., the wall thickness $a = 0.34$ nm. The estimated value of the phase relaxation length L_φ is comparable with the circumference of graphene cylinder, i.e., $L_\varphi \approx 2\pi R$, and is close to that derived by Bachtold et al. [5] on

individual MWNT at $T = 0.3$ K. Theory also points out that the phase of the oscillations, i.e., $\max R$ for $H = 0$, will be reversed by the presence of spin-orbit scattering. In our case, phase reversal does not happen, indicating that spin-orbit scattering is negligible.

Therefore, we conclude that quantum-interference corrections to the resistance can account for the measured longitudinal MR. The good agreement between theory and experiment give a convincing proof that the electric current flows in the outermost metallic graphene wall of MWNTs at low temperatures.

5.3 Summary

Transport properties, including thermoelectric power (TEP) and longitudinal magnetoresistance (MR), have been investigated on millimeter-long aligned multiwall carbon nanotubes (MWNTs). A large and positive TEP with a nearly linear temperature dependence is observed, indicating that the electron-hole symmetry in metallic nanotubes is broken. The low-temperature longitudinal MR of MWNTs shows an oscillation behavior, which is attributed to Altshuler-Aronov-Spivak (AAS) effect. This gives clear evidence that quantum interference phenomena dominate the MR at low temperatures. The phase relaxation length L_φ is found to be comparable with the circumference of the outmost graphene wall. The observation of resistance jumps at integer multiples of $h/2e^2$ suggests that MWNTs are mesoscopic conductors with finite conduction channels.

Bibliography

- [1] J. Hone, I. Ellwood, M. Muno, A. Mizel, M. L. Cohen, A. Zettl, A. G. Rinzler, and R. E. Smalley. Thermoelectric power of single-walled carbon nanotubes. *Phys. Rev. Lett.*, 80:1042, 1998.
- [2] B. L. Al'tshuler, A. G. Aronov, and B. Z. Spivak. The Aaronov-Bohm effect in disordered conductors. *JETP Lett.*, 33:94, 1981.
- [3] B. L. Al'tshuler, A. G. Aronov, B. Z. Spivak, D. Y. Sharvin, and Y. V. Sharvin. Observation of the Aaronov-Bohm effect in hollow metal cylinders. *JETP Lett.*, 35:588, 1982.
- [4] A. G. Aronov and Y. V. Sharvin. Magnetic flux effects in disordered conductors. *Rev. Mod. Phys.*, 59:755, 1987.
- [5] A. Bachtold, C. Strunk, J.-P. Salvetat, J.-M. Bonard, L. Forró, T. Nussbaumer, and C. Schönenberger. Aharonov-Bohm oscillations in carbon nanotubes. *Nature*, 397:673, 1999.

Chapter 6

Conclusions

Main conclusions from our studies on the thermal and electrical properties of MWNTs are as follows:

1. The phonon structure of a MWNT with diameter of several tens of nm is two-dimensional. The inter-wall interactions in a MWNT is very weak, so that one can treat a MWNT as a few decoupled two-dimensional (2D) single wall tubules.

2. The low thermal conductivity indicates that large amounts of defects exist in the MWNTs derived by thermal decomposition method.

3. Strong Coulomb blockade induced zero-bias suppression of tunneling density of states (TDOS) is observed in single tunnel junctions between MWNTs and a normal metal. Quantitative analysis by Environmental Quantum Fluctuation (EQF) theory found excellent agreement with experimental data. A universal exponent $\alpha \approx 0.25\text{--}0.35$ is attributed to strong intratube Coulomb interaction in MWNTs. In low-impedance junctions, Fano-resonance like asymmetric conductance anomaly is found below mV energy scales.

4. The thermoelectric power (TEP) of MWNTs is moderately large. At low temperatures, TEP has a metallic-like linear temperature dependence. Such a large positive thermoelectric power of MWNTs gives strong evidence that the electron-hole symmetry in metallic nanotubes is broken.

5. The longitudinal magnetoresistance (MR) of MWNTs shows an Altshuler-Aronov-Spivak (AAS) effect induced oscillation at 20 mK. This result gives clear evidence that quantum-interference dominate the resistance of MWNTs at low temperatures. The estimated value of the phase relaxation length L_φ is comparable with the circumference of

the graphene cylinder.

致 谢

本论文是在我的导师吕力研究员的悉心指导和关怀下完成的。吕老师敏锐的物理直觉、严谨的治学态度、身先士卒的工作作风和博大的胸怀对我产生了深刻的影响。两年的研究经历极大地开阔了我的视野，锻炼了我的独立思考和动手能力。我取得的每一点进步都凝聚了吕老师的艰辛劳动和大量心血。在这里谨向吕老师致以衷心的感谢。还要特别感谢张殿琳老师在实验方案方面给予我的直接指导和帮助。张老师渊博的学识、活跃的学术思想使我受益非浅。在研究过程中，物理所412组的解思深研究员、潘正伟博士不仅提供了样品，还给予了积极的合作和大力支持，作者向他们表示感谢！感谢清华大学物理系范守善教授、物理所陶宏杰老师、孙刚老师、胡占宁老师在百忙之中抽时间与我讨论实验结果并提出了宝贵的建议。感谢清华大学物理系博士生胡辉同学和本组博士生何海丰同学在碳纳米管的隧道谱方面的有益的讨论。感谢物理所502组潘明祥老师、赵德乾老师、509组赵士平老师、王瑞峰同学和杜寰同学在实验设备和样品制备方面提供的热情帮助。在硕士学习期间，本人得到了本研究组的林淑媛老师、李山林老师、景秀年老师和王云平老师的热情指导和帮助，以及刘恩生、何海丰、赵彦明、刘淑梅、林岚五位同学的大力支持与帮助。作者向他们表示衷心的感谢。在物理所507组度过的时光是难忘的。最后，感谢我的女友陈玉两年来的理解和支持。感谢我的父母以及所有的亲属对我的关怀和帮助！

谨把本文献给我亲爱的父母

Acknowledgments

This dissertation could not have been completed without the meticulous guidance and care of my supervisor, Prof. Lu, Li. Prof. Lu's sharp scientific intuition; strict work attitude; leading roles in experiment; and open mind have deeply affected me. Two years of research experience greatly broadened my horizons, tempered my ability of independent thinking and first-hand skills. Every point of my progress embodies Prof. Lu's painstaking efforts. Here I would like to express my heartfelt gratitude to him.

Special thanks to Prof. Zhang, Dianlin for his direct guidance and help on the experimental schemes. I greatly benefited from Prof. Zhang's vast knowledge and active academic thinking. In the course of my study, Prof. Xie, Sishen and Dr. Pan, Zhengwei at Group 412 not only have provided samples, but also have given enthusiastic cooperation and strong support, I am very grateful to them.

I want to thank Prof. Fan, Shoushan at Physics department, Tsinghua University; Prof. Tao, Hongjie; Sun, Gang; and Hu, Zhanning at Institute of Physics; for spending time with me despite their busy schedules to discuss the experimental results and having made valuable suggestions. I am also thankful to Ph.D. candidate Hu, Hui at Physics department, Tsinghua University; and Ph.D. candidate He, Haifeng in my group; for the helpful discussions on the tunneling spectroscopy measurements.

Thanks to Prof. Pan, Mingxiang and Zhao, Deqian at Group 502; and Prof. Zhao, Shiping; Ph.D. candidates Wang, Ruifeng and Du, Huan at Group 509 for their help in the laboratory equipments and sample preparations.

Many thanks to Dr. Lin, Shuyuan; Li, Shanlin; Jing, Xiunian; and Wang, Yunping in my group for their guidance and support throughout my M.S. study. I am also thankful to my fellow group members Liu, Ensheng; He, Haifeng; Zhao, Yanming; Liu, Shumei; and Lin, Lan for their support and help. The time I spent at Group 507, Institute of Physics is cherishable.

Finally, I would like to thank my girlfriend Chen, Yu for her understanding and support in the past two years. This dissertation is dedicated to my parents for their ubiquitous care and love throughout my life.

Revision Notes

This dissertation is revised from the original version submitted seven years ago. At the time I had not learned how to include figures in LaTeX. Instead, figures were hard copied and the thesis was submitted in printed format only. The main purpose of the revision is to reserve a digital copy and make it available online for interested readers. For authenticity, the main content of the thesis is kept As Is, except for the necessary corrections and reformatting. Noticeable changes are listed as follows:

1. Chapter 4 (Tunneling Spectroscopy) is updated according to the recent publication (PRL 91, 076801 (2003)). The corresponding part in Abstract is updated as well.
2. In Chapter 1, Fig. 1.3(b) is changed. Original figure (curves of constant energy of graphene sheet) is changed to the current version (DOS of carbon nanotubes from STM and tight-binding calculations). Fig. 1.5 is corrected. Original figure (band structure of (5, 5) nanotubes) is replaced by band structure of (10, 10) nanotubes to make it consistent with the context.
3. In Chapter 2, two new figures (Fig. 2.1 and 2.4) are added as complementary materials. Fig. 2.3 is replaced by the published version from Ref. [3].
4. In Chapter 3, Fig. 3.3 (from Ref. [22]) is replaced by more recent data (from Ref. [17]). Fig. 3.5 and 3.9 (omitted in the original thesis) are now included.
5. In Chapter 5, Fig. 5.1 (configuration for TEP measurement) is redrawn to include more details.
6. Summary sections are added for Chapter 2 and Chapter 5.
7. English translation of Acknowledgments is added.

A recent survey by Michael Banks at the Max Planck Institute has ranked carbon nanotubes as one of the top five topics in physics publications. Although this does not promise that someday they would replace silicon microelectronics, or make space elevators, carbon nanotubes and related materials remain attractive for both fundamental research and potential applications. Since the nanotube research is evolving very fast, the content of this thesis may become obsolete. Somehow I still feel obligated to finish the revision, not

just for fun, but also to make a repository of the pleasant memories of my first scientific safari.

Wei Yi

Cambridge, Massachusetts

Aug. 2006